ABSTRACT

Title of dissertation: Explorations of Variable Interactions in a Cold Rubidium Rydberg Gas

Jennifer E. Robinson, Doctor of Philosophy, 2012

Dissertation directed by: Professor Steven Rolston
Department of Physics

We explore dipole-dipole interactions between cold ^{87}Rb Rydberg atoms, their utility for quantum computing, and their potential role in the development of exotic quantum phases in optical lattice systems. Rydberg atoms can have large dipole-dipole interactions, due to the fact that they are easily polarized. We propose a new atomic state, created by admixing the Rydberg state with the ground state, in order to create an atom with a long lifetime and an intermediate dipole moment, which would be useful for experiments in optical lattices. These states could be used to probe phases of the extended Bose-Hubbard Hamiltonian, as well as create novel R-dependent interactions that are not realizable in conventional condensed matter systems. In addition to the dressed-Rydberg states, we consider the use of external DC electric fields to produce a variable interaction strength. A Stark map of the specific Rydberg levels shows the energy shift of a Rydberg atom in an electric field, as well as the dipole moment, from the slope of the curve. We study Rydberg excitation in an intermediate density regime under the effects of a variable external static electric field. We use superatom analysis and Monte Carlo simula-

tions of a Rydberg system with dipole blockade to determine that our experimental observations are consistent with an increasing dipole-dipole interaction due to an induced dipole moment, with an enhancement due to black-body-induced transitions to nearby higher-angular-momentum states. We also investigate the Van der Waals interaction by considering the zero-field excitation rate for multiple principle quantum numbers.

EXPLORATION OF VARIABLE INTERACTIONS IN A COLD RUBIDIUM RYDBERG GAS

by

Jennifer E. Robinson

Dissertation submitted to the Faculty of the Graduate School of the
University of Maryland, College Park in partial fulfillment
of the requirements for the degree of
Doctor of Philosophy
2012

Advisory Committee:
Professor Steven Rolston
Professor Chris Monroe
Dr. Eite Tiesinga
Dr. Gretchen Campbell
Professor John Fourkas, Dean's Representative

Dedication

To Mrs. Piwko, who taught me to THINK!

Acknowledgments

I would like to thank the previous members of the Rb BEC lab for building the MOT apparatus and teaching me to use it, especially Matthew Beeler and Emily Edwards. I would like to thank Ilya Arakelyan for his help and guidance designing the stable blue laser setup and Takuma Inoue for his further assistance. I would like to thank Tao Hong for his help in writing the code to calculate the Stark map of the Rydberg atoms, and Zach Smith for helping me keep the lasers locked when I was desperately trying to take more data this year. I would also like to acknowledge useful conversations with Trey Porto, Sankar Das Sarma, Eite Tiesinga, and Guido Pupillo, as well as Gretchen Campbell for her advice. And of course, I'd like to thank my advisor, Steve Rolston.

I would also like to thank my family and friends for all their love and support.

Table of Contents

List of Tables

List of Figures

List of Abbreviations

JQI	Joint Quantum Institute
NIST	National Institute for Standards and Technology
n	principle quantum number
l	orbital angular momentum
DDI	dipole-dipole interaction
MOT	magneto-optical trap
BEC	Bose-Einstein condensate
a_0	the Bohr radius
e	electron charge
k_B	Boltzmann's constant
h	Planck's constant
AOM	acousto-optical modulator
EOM	electro-optical modulator

Chapter 1

Introduction

1.1 Overview

Rydberg atoms are atoms in which the valence electron has been excited to a high principal quantum number. Because of the large orbit, the Rydberg atom is easily polarized and can have a dipole moment on the order of $n^2 e a_0$, where n is the principal quantum number and a_0 is the Bohr radius. This dipole moment is several orders of magnitude larger than that of a ground-state atom. Additionally, Rydberg atoms can have interactions much larger than those between ground-state atoms, even magnetically dipolar atoms. Because of their large interaction energies, Rydberg states have been considered as a way to implement quantum gates between two neutral atoms [32]. Dipole-dipole interactions (DDIs) have also been proposed as a mechanism with which to study novel quantum phases because of their long-range and anisotropic qualities.

1.2 Rydberg Atoms

Rydberg atoms appear in Johann Balmer's formula for the wavelengths of the visible spectrum of atomic hydrogen, which describes the transitions of the hydrogenic electron from $n = 2$ to higher lying states [21, 61]. George Liveing and

James Dewar expanded this understanding of atomic spectra to include the alkali atoms sodium and potassium. Johannes Rydberg used this work to begin classifying the spectra of other atoms, most notably the alkali atoms, into a series of discrete lines. He discovered that the atomic lines of various alkali atoms could be expressed universally as

$$\nu_{nl} = \nu_{\infty l} - \frac{Ry}{(n - \delta_l)^2}, \tag{1.1}$$

where $\nu_{\infty l}$ is the energy limit of the series for a given angular momentum l, δ_l is the the quantum defect, which is independent of n, and Ry has come to be known as the Rydberg constant. This is constant not only for different angular momenta, but also for different atoms. In 1896, Rydberg discovered, in parallel with Arthur Schuster, that the $\nu_{\infty l}$ values follow the relation

$$\nu_{\infty p} - \nu_{\infty s} = \nu_{1p} = -\nu_{0s}. \tag{1.2}$$

This expression has become known as the Rydberg-Schuster Law [61].

When Bohr proposed his model of the hydrogen atom, the significance of high n became more apparent, as the Bohr model includes the interesting properties of high-n Rydberg atoms as well [21]. Because the valence electron orbits far away from the positively charged core, Rydberg atoms are approximately hydrogenic, except for the quantum defect, which describes a small deformation of the electron cloud and falls off quickly with increasing angular momentum.

1.3 Rydberg Atom Interactions

The large distance of the Rydberg atom's valence electron from its positively-charged core yields interesting long-range interactions between different Rydberg atoms. The atom is highly susceptible to polarization and can exhibit strong DDIs, as well as large van der Waals interactions. The van der Waals interaction in Rydberg atoms is not as long-range as the DDI, but is still orders of magnitude stronger than those of ground-state atoms. There are multiple phenomena that modify long-range interactions in Rydberg atoms, the mostly commonly studied of which are Förster resonances [60] and the Stark effect [59].

Förster resonances arise from collisional interactions between Rydberg atoms that couple one angular momentum state with states of angular momentum differing by one unit. This coupling effectively breaks the parity of the state and can give rise to a DDI term in the interaction. The collision

$$nl + nl \rightarrow n'l' + n''l'' \tag{1.3}$$

has a Förster resonance when $l', l'' = l \pm 1$, where angular momentum is conserved by considering that $m'_l + m''_l = 2m_l$, and

$$2E_{nl} = E_{n'l'} + E_{n''l''}. \tag{1.4}$$

Using a two-state Hamiltonian and the DDI between the Rydberg states leads to an interaction energy described by the expression

$$U_{\pm}(R) = \frac{\Delta}{2} \pm \sqrt{\frac{4U_3(R)^2}{3} + \frac{\Delta^2}{4}} \tag{1.5}$$

where $\Delta = E_{n'l'} + E_{n''l''} - 2E_{nl}$ and $U_3(R) = e^2\langle nl||r||n'l'\rangle\langle nl||r||n''l''\rangle/R^3$, which represents an anisotropic DDI. The r matrix elements contains the angular dependence of the dipole moment, which combine to produce an anisotropic potential in three dimensions. This expression converges to a DDI $\sim 1/R^3$ for small values of Δ, and converges to a van der Waals like interaction $\sim 1/R^6$ at large values of R. This shows how Förster resonant states can give rise to DDIs. Förster resonances can either occur incidentally for certain Rydberg states, or else be tuned using effects that deflect even- and odd-parity energy levels with opposite signs, such as the Stark effect [60].

The Stark effect, which I will discuss in more detail in Chapter 2, can also give rise to strong, permanent dipole moments. The DC Stark effect occurs when an atom interacts with a static, externally-applied electric field [50]. The Stark effect Hamiltonian is given by $H' = -\vec{E} \cdot \vec{d}$. Because the dipole operator is given by $e\vec{r}$, the electric field yields the result that opposite-parity eigenstates will mix, causing a dipole moment that depends upon the magnitude of the electric field. For small fields, this Stark-shifted energy is quadratic in electric field, producing a dipole moment that is linear in field. For large fields, the shift is linear in field, creating a constant, permenant dipole moment for all large fields [50].

Förster resonances and the Stark effect are ways in which long-range DDIs can arise in systems of Rydberg atoms. These strong, long-range interactions are

interesting for many reasons, particularly in the development of quantum logic gates and the study of novel quantum phases of matter.

1.4 Quantum Logic Gates

Quantum computing has gained attention recently as a way of making computers using the properties of quantum states [55]. In classical computing, the unit of information is a bit, a binary state that can be either in state 1 or state 0. In quantum computing, the quantum bit, or qubit, is a quantum state, described by state $|1\rangle$ or $|0\rangle$. Because of the principle of superposition, the qubit can actually take the value of any normalized superposition of states $|1\rangle$ and $|0\rangle$. This effect, along with the exponential scaling of the Hilbert space, allows more information to be stored in a collection of qubits than in classical bits. It is postulated that with a quantum computer, one could reduce the time it takes to perform some classically intractable calculations from a time that scales exponentially with the problem size to one that scales polynomially [53].

Additionally, the principle of entanglement can lead to encryption that is unbreakable to an outside eavesdropper. Entanglement can also be used to design encryption protocols that would reveal any eavesdroppers before they can do harm. Entanglement occurs when two bits are in a state such that measuring the state of one atom automatically reveals the state of the other. Entangled states are often described as a non-factorizable superposition of quantum states, such as $|0\rangle|0\rangle + |1\rangle|1\rangle$, although it is possible to entangle more than one state at a time. If one were to

measure one of these bits, then one would also know the state of the others instantaneously.

In order to implement a quantum computer, it is necessary to have qubits, operations that can affect a single qubit, and conditional logic gates that affect two or more qubits. The Rydberg state can be used to implement a two-qubit quantum gate, as described in [32].

1.5 Rydberg Blockade

One method of creating a quantum conditional logic gate, described in [32], is by using the Rydberg blockade effect. Rydberg blockade describes the phenomenon whereby the Rydberg-Rydberg interaction shifts the energy of the doubly-excited state out of resonance with the excitation laser, thereby preventing a nearby second atom from being excited to the Rydberg state at the same time [57].

When DDIs are present, such as in the presence of an electric field or Förster resonance, the interaction between Rydberg atoms scales as c_3/r^3, where c_3 depends upon the magnitude of the dipole moment and r is the separation between atoms; in the absence of a dominant DDI, the van der Waals interaction dominates and falls off as c_6/r^6. When two atoms are excited from a ground state to the Rydberg state, this interaction shifts the energy levels of the atoms, acting like a detuning from resonance. When this detuning is greater than the linewidth of the Rydberg transition, excitation of two atoms to the Rydberg state with a laser tuned to the one-atom resonance is strongly suppressed. This phenomenon is known as blockade.

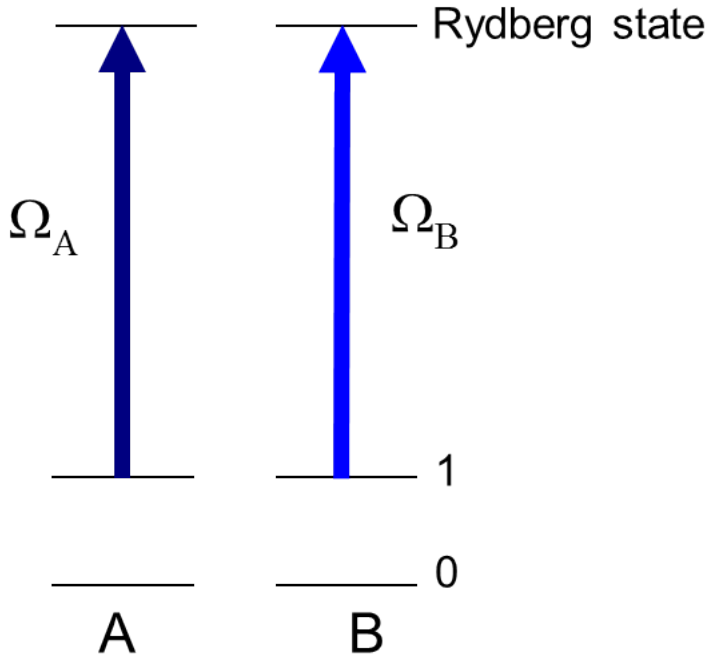

Figure 1.1: A schematic for creating a quantum conditional logic gate using Rydberg blockade. Ω_i represents the laser frequency that addresses atom i, where i is A or B.

Because the interaction energy falls off as $1/r^3$ (or $1/r^6$), there is a radius around an excited Rydberg within which no other atom can be excited to the Rydberg state at the same time. This distance is known as the blockade radius.

Jaksch, et al. [32], describe a gate operation by which the Rydberg blockade phenomenon can be used to implement a two-qubit quantum gate. Consider the arrangement in Fig. 1.1, where atoms A and B each have two ground sublevels, such as hyperfine levels, $|0\rangle$ and $|1\rangle$, where $|1\rangle$ is coupled to a Rydberg state by a laser with frequency Ω_i where i is A or B. This protocol, shown in Fig. 1.2, assumes individual addressability, where Ω_A and Ω_B represent the laser that addresses atoms

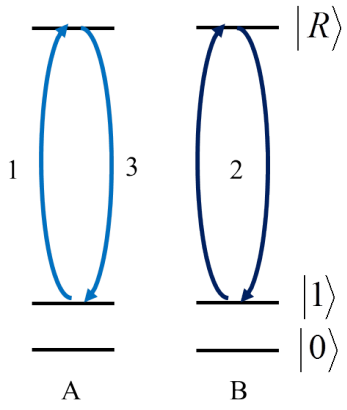

Initial	Step 1	Step 2	Step 3
00	00	00	00
01	01	-01	-01
10	R0	R0	-10
11	R1	R1	-11

Figure 1.2: The operation protocol for the gate described in the previous figure. Gate operation involves applying a π-pulse to atom A, a 2π-pulse to atom B, and another π-pulse to atom A. The table describes each atom's state after each step, for all four possible initial states. The Rydberg blockade causes this protocol to yield a conditional phase gate, as atom B is not excited during step 2 for the intial state 11.

A and B, respectively. To implement the gate, one first applies a π-pulse of Ω_A, then a 2π-pulse of Ω_B, and finally another π-pulse of Ω_A. In the situation where both atoms begin in state $|1\rangle$, the intial excitation of atom A to the Rydberg state blockades atom B, so that it does not get excited and de-excited. When atom A receives another π-pulse, it returns to state $|1\rangle$, causing a 2π phase shift, rather than the 4π shift that would result in the absence of blockade. The result is that if both atoms start out in state $|0\rangle$, then the gate causes no change to the state, but if they start out in any other combination of initial states, the system picks up a 2π phase shift. This scheme can be combined with single-qubit rotations to produce a controlled-NOT gate, which would preserve this conditional phase shift, thereby performing the operations necessary to create a quantum computer.

It is also possible to use Rydberg blockade to create an entangled state, as in Fig. 1.3. If, instead of tuning to the single-Rydberg resonance, we were to tune the excitation laser to be detuned by a single interaction energy, we could excite two atoms to the state $|\psi\rangle = |00\rangle + |11\rangle$, where the two atoms can only be both in the ground state, or both excited, but not be in the state where one is excited and the other is not. Because the interaction depends on r, this would require a fixed internuclear distance, and would probably only be possible with atoms in an optical lattice.

The Rydberg blockade phenomenon, however, is not a sharp-edged effect. While atoms close enough to have an interaction energy greater than the transition linewidth are likely to be blockaded, the interaction itself varies smoothly from short distances to long. Additionally, in a gas, while the atoms may have some av-

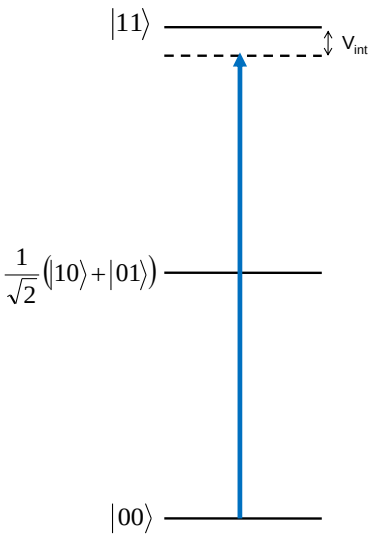

Figure 1.3: A schematic for creating an entangled state using Rydberg blockade. The state $|11\rangle$ represents both the atoms in the Rydberg state, so that a laser tuned to the interaction-shifted two-atom resonance will excite the atom to a state where both atoms can be either in the ground or Rydberg state.

erage internuclear spacing related to the density, in reality all possible r in a given system are statistically present, leading to a muddying of the blockade effect. In this intermediate regime, it is possible to study the emergence of the blockade phenomenon by investigating clouds where the interaction is strong enough to suppress the Rydberg excitation rate, but not strong enough to blockade the excitation entirely. Because the DDI is longer-range than the van der Waals interaction, dipolar quantum particles are useful for studying quantum phases that arise due to longer-range interactions.

1.6 New Quantum Phases

Systems of Bose condensed atoms in optical lattices are a way to model solid state systems [10]. They provide an experimental system with minimal defects and great control over the experimental parameters. Experimental groups have observed the superfluid-to-Mott-insulator transition predicted by the Bose-Hubbard model with nearest-neighbor interactions [25]. Recent theoretical work has focused on extending the Bose-Hubbard model to include interactions beyond nearest neighbors [23, 51, 36]. Most neutral atoms trapped in optical lattices interact mainly by Van der Waals forces, which have a short range and are well-modeled with a contact interaction. The interactions among trapped, non-dipolar atoms typically occur only between atoms on the same site. In systems of particles that interact via longer-range forces, like the dipole-dipole force, interactions could take place between particles on different sites.

[23], [47], and [46] suggest possible systems in which one could study phases of cold bosons with long-range interactions. These systems include polar molecules, atoms with permanent magnetic or electric dipole moments, and cold Rydberg atoms [23]. While some groups have explored polar molecules [42] and atoms with a large magnetic dipole moment [26], Rydberg atoms with defined dipole moments offer an interesting alternative direction. The interaction strength between Rydberg atoms can be controlled and tuned over a large range of values, in comparison to the interaction strength of the set dipole moments of polar molecules. [1] describes the trapping of Rydberg atoms in an optical lattice. Additionally, the possibility of trapping Rydberg-dressed states in an optical lattice will be discussed in Chapter 3.

The traditional Bose-Hubbard model [32, 18] describes interactions between bosons in a periodic potential, or lattice. Interactions occur only when two or more atoms occupy the same lattice site. Atom hopping from one site to another also affects the system. The model does not allow for interactions between atoms on different sites of the lattice. Extending the Bose-Hubbard Hamiltonian by adding further terms allows atoms to interact with atoms on neighboring sites. In this new model, there are terms that describe the interaction of atoms with their nearest neighbors, next nearest neighbors, and so forth.

The extended Bose-Hubbard Hamiltonian takes the form [23]

$$H = J\sum_{\langle i,j\rangle} b_i^\dagger b_j + \frac{1}{2}U_0\sum_i n_i(n_i-1)$$
$$+\frac{1}{2}U_{\sigma_1}\sum_{\langle i,j\rangle} n_i n_j + \frac{1}{2}U_{\sigma_2}\sum_{\langle\langle i,j\rangle\rangle} n_i n_j + ... \tag{1.6}$$

where J is the hopping coefficient, b_i is the annihilation operator for the i^{th} site, $b_i^\dagger$

is the creation operator at the i^{th} site, $n_i = b_i^\dagger b_i$ is the number of atoms on the i^{th} site, U_0 is the on-site interaction energy, $\langle i,j\rangle$ describes a sum over nearest neighbors with interaction energy U_{σ_1}, and $\langle\langle i,j\rangle\rangle$ describes a sum over next-nearest neighbors with interaction energy U_{σ_2}. Further terms describe longer-range interactions.

The Wannier functions $w(\vec{r}-\vec{r}_i)$ can be used to describe the wavefunction of a particle on the i^{th} site, where $\vec{r}_i$ is the position of the minimum of the site potential well. We can find the hopping coefficient, J, by finding the overlap of the Wannier functions of neighboring sites.

The off-site interaction comes from

$$U_{\sigma_m} = \int |w(\vec{r}-\vec{r}_i)|^2 V_{int}(\vec{r}-\vec{r}')|w(\vec{r}'-\vec{r}_j)|^2 d^3r d^3r' \tag{1.7}$$

where $|\vec{r}_i-\vec{r}_j| = 4\pi\sigma_m/|\vec{k}|$, where $|\vec{k}|$ describes the periodicity of the lattice potential. Different subscripts m describe how close the neighbor is to the considered site, where $\sigma_1 = 1, \sigma_2 = \sqrt{2}, \sigma_3 = 2$, and $\sigma_3 = \sqrt{5}$ on a square, 2D lattice, for example.

A system with both dipole-dipole interactions and van der Waals interactions, has a potential of the form

$$V_{int} = d^2\frac{1-3cos^2\alpha}{|\vec{r}-\vec{r}'|^3} + \frac{4\pi\hbar^2 a}{m}\delta(\vec{r}-\vec{r}'), \tag{1.8}$$

where d is the dipole moment, $\vec{r}$ and $\vec{r}'$ are the position vectors of the two dipoles, α is the angle between them, and a is the s-wave scattering length for ground-state atoms. The potential can change from attractive to repulsive depending on the value of α. The anisotropy, as well as the strength, of these interactions can lead to new phases

of matter. The delta-function term describes the $\sim 1/r^6$ van der Waals interaction between ground-state atoms as approximately equal to a contact interaction because this interaction decreases much faster with increasing r compared to the DDI term. There can also be van der Waals interactions between Rydberg atoms in the system, which may vary as $1/r^5$, as described in [54].

If the interactions are isotropically repulsive and strong, the system will prefer to be in a state in which the atoms prefer not to occupy lattice sites that have an occupied nearest neighbor, leading to a checkboard phase [23, 51]. If the interactions are anisotropic (more repulsive in one direction than in another)a striped phase will result. These long-range interactions can also lead to a phase where the atoms are localized in lattice sites, but maintain coherence among the sites, such that the density matrix has both long-range diagonal and off-diagonal order. This phase is called a supersolid phase. While groups claim to have observed this phase in condensed matter systems [34], the results are controversial [45]. This phenomenon has yet to be studied in an optical lattice system, which is free of impurities and disorder, and could have a clear, definitive signature.

Additionally, a recent paper [47] has suggested the emergence of quantum phases in two-dimensional systems of dipolar particles. They assume a cloud of dipolar particles of mass m, confined to a two-dimensional, symmetric harmonic trap with trapping frequency ω, and then define the length and energy scales $r_0 = (\tilde{D}/m\omega^2)^{1/5}$ and $\tilde{\epsilon} = m\omega^2 r_0^2 = \tilde{D}/r_0^3 = (m^3\omega^6\tilde{D}^2)^{1/5}$, where $\tilde{D}$ is the DDI coefficient proportional to $|\vec{d}|^2$, which yields a new 2D Hamiltonian,

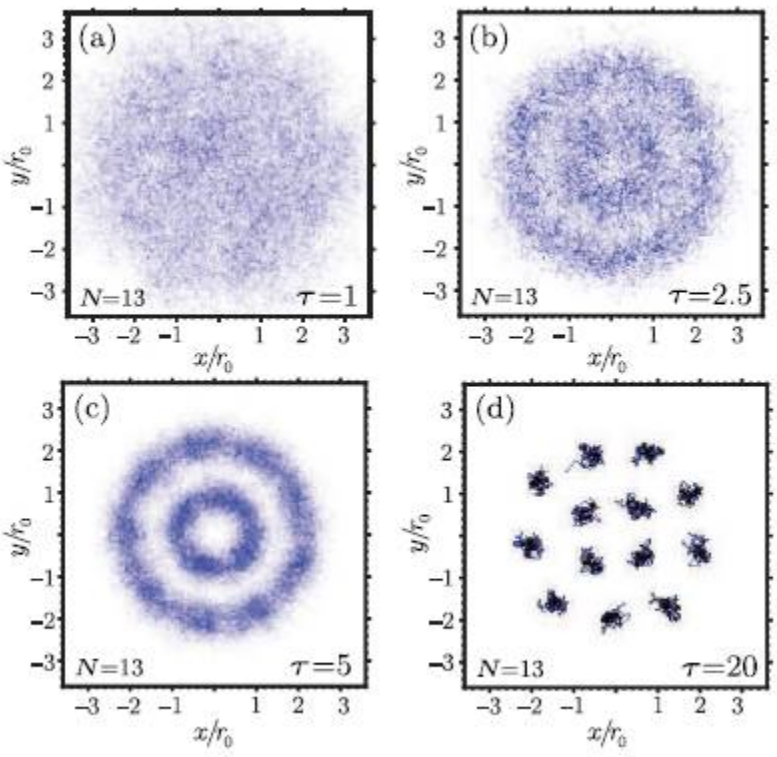

Figure 1.4: The transition from superfluid to Wigner Crystal via the supersolid phase, as shown by emergent order in the density of particles. From [47]

$$\frac{H}{\tilde{\epsilon}} = \sum_{i=1}^{N}[-\frac{1}{2\tau^2}\frac{\partial^2}{\partial\rho_{\mathbf{i}}^{\mathbf{2}}} + \frac{1}{2}\rho_i^2] + \sum_{i>j}\frac{1}{|\rho_i - \rho_j|^3}, \tag{1.9}$$

where $\tau \equiv \tilde{\epsilon}/\hbar\omega = (r_0/l)^2$ characterizes the strength of the dipole-dipole interaction in a harmonic trap with harmonic oscillator length $l = \sqrt{\hbar/m\omega}$. This Hamiltonian shows that τ in this system plays the role of an effective mass, which can be increased by increasing interactions or compressing the trap.

Figure 1.4 shows a Monte-Carlo simulation of this system for $N = 13$ [47]. As τ increases, the higher densities of particles becomes more likely to be found at specific locations in the trap, localizing into a shell structure at first, and then

into a self-ordered crystal. At intermediate values of τ, the particle density shows characteristics of both the dipolar crystal, as well as of the superfluid, unlocalized cloud. This suggests the existence of a supersolid phase at intermediate values of the interparticle interactions. While the interactions between Rydberg atoms are much stronger than those considered in the paper, there is the possibility that an atom could be dressed in a superposition of the Rydberg and ground state, providing a long-lived state with interactions that are controllable by changing the parameters of the dressing beam. This situation will be discussed further in Chapter 3.

A later work [12] finds that even a blockaded cloud has interesting interactions that could lead to the formation of a supersolid phase. In an ensemble with an interaction that becomes approximately flat at a certain range, with a dipolar long-range tail, the atoms will begin to self-assemble as the thermal interactions become smaller than the other interactions. In the limit in which the blockade radius is much smaller than the interparticle distance, this system behaves much the same as the one discussed previously. In the case in which the blockade radius is on the same order of the interparticle distance, but slightly larger, the system behaves differently, forming what they call a droplet crystal. A system of non-dressed Rydbergs would fall into this second category.

Figure 1.5 shows the organization of an infinite system of bosons interacting via the stepwise potential for an interparticle spacing that is approximately half the blockade radius. As the images progress from (a) to (d), the temperature, expressed in dimensionless units related to the characteristic strength and extent of the theoretically considered potential, decreases from 200 down to 0.1 and the

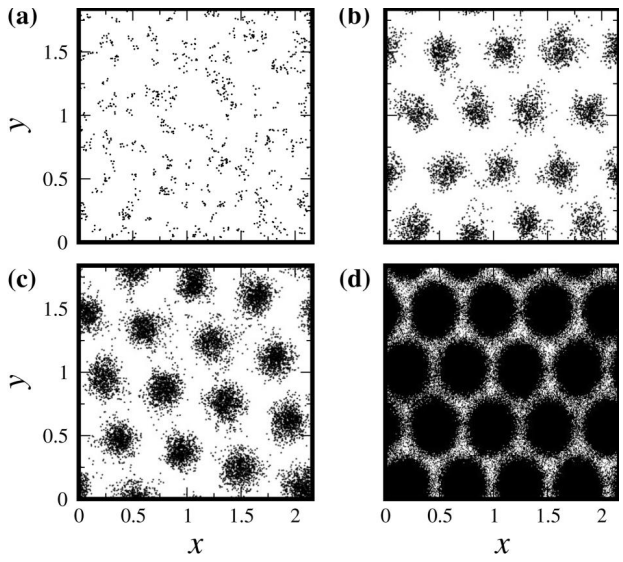

Figure 1.5: The evolution from thermal gas to droplet crystal, from [12].

dipolar interaction dominates over the thermal interactions of the atoms [12]. One can see that the atoms first form a self-assembled crystal structure and then, as the dipolar interaction dominates further, the atoms form what is called a droplet crystal phase, where the atoms form a tightly-bunched triangular lattice with sharply defined minima between the atoms.

1.7 Potential experimental applications

An ensemble of dipolar Rydberg atoms has unique properties that make it attractive for observing these theoretical predictions. Because Rydberg atoms have large dipole moments, it is possible for them to have DDI on the order of GHz. This interaction is much larger than the electric DDI between polar molecules, and stronger even than the DDI between magnetic dipoles such as those in chromium

systems. While polar molecules have been suggested as a potential dipole for these theoretical projects, Rydberg atoms have the advantage of being simpler to produce and having a larger range of interaction strengths that could be probed and controlled. Additionally, recent work has shown that it is possible to trap Rydberg atoms in optical lattices [1], which provides the necessary flexibility of geometry to create both the cigar-shaped traps [36] and the pancake traps [47].

In this thesis, I will present the early steps towards realizing some of the applications of Rydberg atoms to exotic states of matter. Because the interactions in [12] focus on Rydberg atoms in a moderately blockaded regime, we needed to investigate the ways to change the DDIs between Rydberg atoms. This goal can be achieved via a Förster resonance [60], or by applying an external electric field to the atoms [59]. Chapter 2 details our calculations of the Stark effect on Rb Rydberg levels, and how we can use electric field to induce a controlled permanent dipole moment in our system. Chapter 3 shows our calculation of the specific interactions between Rydberg-dressed atoms and how they differ from the naive picture of a weaker dipole interacting via the DDI. We also show that, for some parameters, the interaction takes approximately the form of a stepped interaction that is flat for short distances but falls off as $1/r^3$ at longer range, as is considered in [12] and [29]. In Chapter 4, I will describe our experimental apparatus and how we trap atoms and excite them to Rydberg levels. In Chapter 5, I will report the results of experiments, showing how we can tune the interactions between the Rydbergs with an external electric field for the $50S_{1/2}$ state. We observe this effect by seeing how the excitation rate decreases as we increase electric field, suggesting an increase in

blockade. This technique could be used to realize the system in [12] by changing the field, rather than changing the temperature of the cloud. I will also describe our techniques for data analysis. In Chapter 6, I will report on the results of experiments comparing the blockade as a function of external electric field for different principal quantum numbers. By varying the principal quantum number, we can examine the effects of the field-independent van der Waals interaction on our observed Rydberg excitation.

Chapter 2

Stark Map of Rubidium Rydberg States

2.1 Overview

In order to precisely determine the energy levels and dipole moments of atoms in an external electric field, it is necessary to calculate the Stark shift of the states we wish to use. The Stark effect is well-known to those who have studied introductory quantum mechanics, and calculating the Stark shift of Rydberg states is less complicated because their structure makes them nearly hydrogenic. I calculated the Stark shift of the energy levels relevant to the data taken in Chapters 5 and 6, as well as the resultant dipole moment. This calculation gives us a way to calibrate our experimentally applied electric field, as well as a way to calculate the dipole moment of a given state as a function of the applied field. We can also use the perturbed wavefunctions to find the field-dependent interaction strength for a given Rydberg state.

2.2 Rydberg Atom Wavefunctions

To determine the Stark shift of specific Rydberg levels, it is necessary to calculate the Rydberg atom wavefuntion. The equation of motion for the electron in a Rydberg atom is the spatial Schroedinger Equation:

$$\left(-\frac{\nabla^2}{2}-\frac{1}{r}\right)\psi(r,\theta,\phi)=W_{nl}\psi \tag{2.1}$$

where W_{nl} is the energy of the state. Because the potential depends only on the distance between particles, the angular part of the wavefunction remains the spherical harmonic functions, as in the Hydrogen atom wavefunction. It remains to determine the radial wavefunctions, $R(r)$ of the states that are accessible by laser excitation, which solve

$$\frac{\partial^2 R}{\partial r^2}+\frac{2}{r}\frac{\partial R}{\partial r}+\left(2W_{nl}+\frac{2}{r}-\frac{l(l+1)}{r^2}\right)R=0. \tag{2.2}$$

In Rydberg states with low orbital angular momentum, the electron orbit will penetrate the nucleus as it orbits. This contact causes the orbit to deform, which perturbs the energy. I can approximate this perturbation to the energy by using an effective principal quantum number $n_{eff}=n-\delta_l$, where δ_l is called the quantum defect, and l is the orbital angular momentum. For larger values of l, where there is little overlap of the electron with the nucleus, the quantum defect decreases, until it becomes negligible for high l. The new allowed energy levels become

$$W_{nl}=-\frac{1}{2n_{eff}^2}=-\frac{1}{2(n-\delta_l)^2} \tag{2.3}$$

where n is the principal quantum number.

I calculate these energies for a given n and l by using quantum defects from [37]. Once I determine the energy of the levels, I make substitutions to write Eq.2.2 in a solveable form. We write $x=\sqrt{r}$ and $Y(x)=r^{3/4}R(r)$, and the equation becomes:

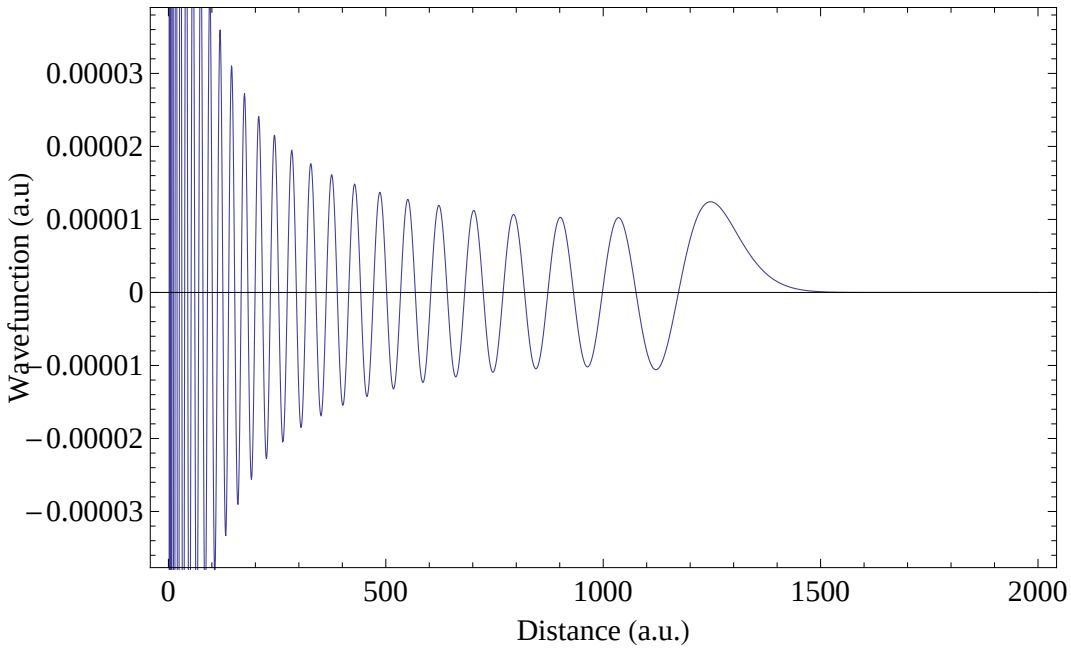

Figure 2.1: The wavefunction for the 55S Rydberg state, as calculated by the method of Bhatti.

$$\left(-\frac{d^2}{dx^2} - 8W_{n,l}x^2 + \frac{\left(2l+\frac{1}{2}\right)\left(2l+\frac{3}{2}\right)}{x^2}\right) Y(x) = 8Y(x) \tag{2.4}$$

I then solve this equation numerically, by integrating from $r = 0$ to inf, assuming that $Y(\text{inf}) = 0$. This wavefunction is then normalized by dividing by the integral over all space of the unnormalized wavefunction, which yields a wavefunction that looks like Fig. 2.1, which shows the wavefunction of the 55S Rydberg state.

2.3 Stark Effect Hamiltonian

Once I have the Rydberg atom wavefunctions, I use them to calculate elements of the dipole interaction matrix. Diagonal terms are give by W_{nl}, while off-diagonal terms come from the interaction with an electric field. The matrix elements are

given by the inner product of the wavefunctions with the Stark effect Hamiltonian:

$$V = \langle n, l, m|\vec{E} \cdot \vec{d}|n', l', m'\rangle \tag{2.5}$$

where $\vec{E}$ is the applied electric field and $\vec{d}$ is the dipole moment. Because $\vec{d} = e\vec{r}$, and I can define $\vec{E} = E\hat{z}$, these off-diagonal elements become

$$V = \langle n, l, m|eEz|n', l', m'\rangle = \langle n, l, m|eErcos\theta|n', l', m'\rangle. \tag{2.6}$$

I can break this expectation value into two integrals. The first integral is the angular part of this expectation value,

$$\int d\phi d(cos\theta) Y^{\star}_{l'm'}(\theta, \phi) cos\theta Y_{lm}(\theta, \phi), \tag{2.7}$$

where the substitution $Y_{10}(\theta, \phi) = \sqrt{3/4\pi} cos\theta$ makes this straightforward to solve[62]. The substitution explicitly shows that transitions will only occur between levels with the same m, and with $l' = l \pm 1$. This selection rul simplifies Eq. 2.7 to

$$\begin{aligned} \langle l, m|cos\theta|l-1, m\rangle &= \left(\frac{l^2 - m^2}{(2l+1)(2l-1)}\right) \\ \langle l, m|cos\theta|l+1, m\rangle &= \left(\frac{(l+1)^2 - m^2}{(2l+3)(2l+1)}\right). \end{aligned} \tag{2.8}$$

The second integral is the radial part of the expectation value,

$$\int dr R_{n'l'}(r) r^3 R_{nl}(r), \tag{2.9}$$

with $R_{nl}(r)$ calculated above.

The angular part of the integral is further complicated, however, by the spin-orbit coupling, which labels states in terms of l, j, and m_j, rather than l and m_l. In order to simplify the angular expectation value, it is necessary to use an alternate expression from [62]:

$$\langle l, j, m_j | cos\theta | l', j', m_j' \rangle = \delta(l, l' \pm 1)\delta(m_j, m_j') \sum_{m_l = m_j = \pm\frac{1}{2}} \langle l, \frac{1}{2}, m_l m_j - m_l | j m_j \rangle$$
$$\times \langle l', \frac{1}{2}, m_l m_j - m_l | j m_j \rangle \langle l, m_l | cos\theta | l' m_l \rangle. \quad (2.10)$$

This expression adds more elements to the Hamiltonian matrix, but can be simplified by the fact that different m_j levels do not couple, and so I can calculate and diagonalize the matrix for each $|m_j|$, using only the values in which we have interest for the experiment. Upon constructing the Hamiltonian matrix, I then diagonalized the matrix to find the energy levels of the system as a function of electric field strength. The S-states, which are the most commonly-used state in this experiment, have only one $|m_j|$ state associated with them, so I show the Stark map for $|m_j| = 1/2$, $l \in [0, 6]$ in Fig. 2.2.

2.4 Energy Levels and Wavefunctions

When I diagonalize the Hamiltonian constructed in the previous section, I get the Stark-shifted energy levels, as well as the perturbed wavefunctions. The energy levels tell me how the energy of the Rydberg state will shift as I turn up the electric field, thereby telling me how much applied electric field is needed in order to detune the resonance by a certain amount.

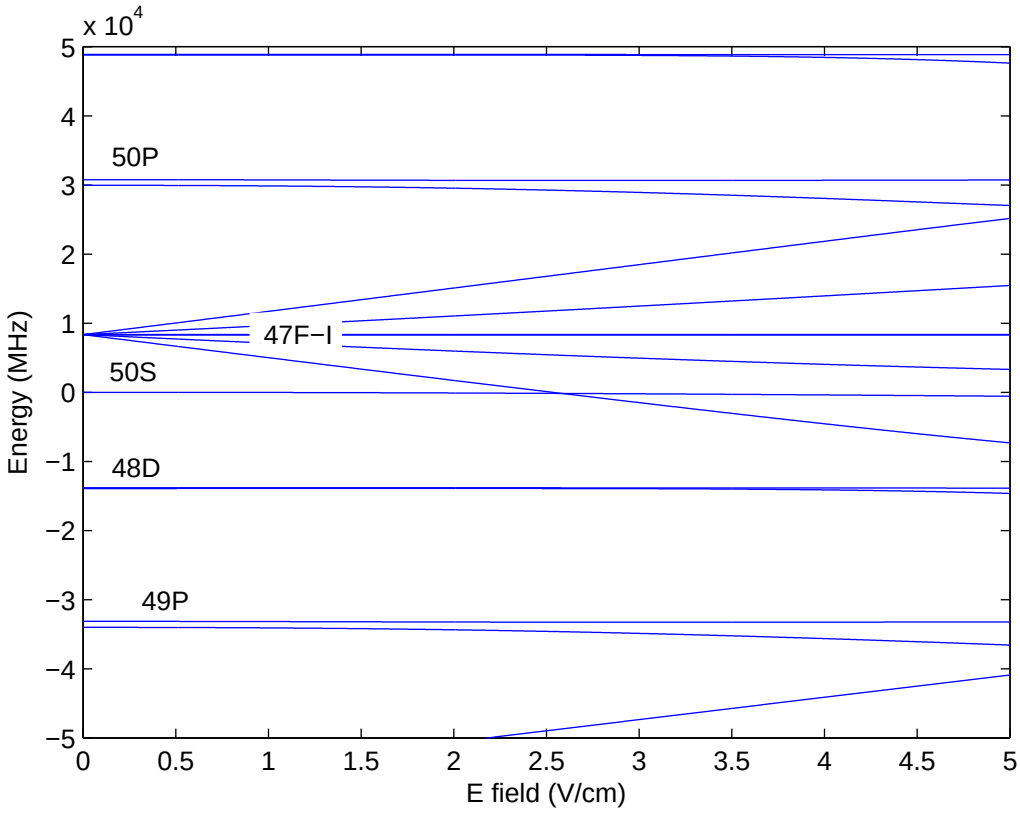

Figure 2.2: A map of the Stark-shifted levels, centered around the $50S_{1/2}$ state.

For small electric fields, the energy shift is given in [50] as:

$$\Delta = -\frac{1}{2}\alpha E^2 \tag{2.11}$$

where E is the magnitude of the electric field and α is the polarizability of the electric field. This shift describes the regime where the Rydberg atom is polarized by the external field, and produces a field-dependant interaction. From the original expression for the Stark shift, I can deduce that the dipole moment should vary with the dervative of the energy with respect to field, so the dipole moment should be linear in the applied field.

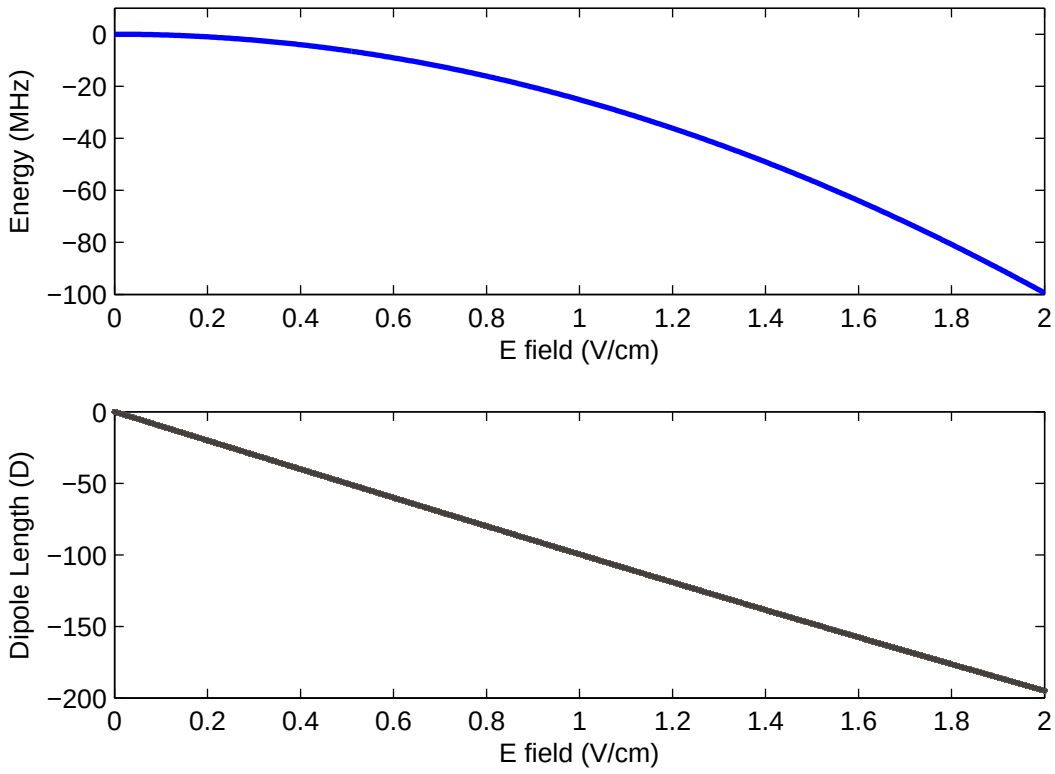

Figure 2.3: The Stark energy shift and induced dipole moment for the $50S_{1/2}$ state of Rb.

I also can calculate the new eigenfunctions for non-zero electric fields. These wavefunctions will be linear combinations of the unperturbed wavefunctions:

$$|\psi_{Stark}\rangle = \Sigma c_i |nlm_l\rangle_i \tag{2.12}$$

where $|nlm_l\rangle$ is the unperturbed wavefunction and the coefficients c_i will depend upon the applied electric field. If I were to take the expectation value of the dipole operator, er, using any of these unperturbed wavefunctions, it would be zero by symmetry. Applying an external field, however, mixes in states of differing parity, causing the expectation value of the dipole operator to be non-zero, as shown in Fig. 2.3 for the $50S_{1/2}$ state. As is apparent in the figure, the parabolic curve of the energy shift, and the linear relationship of the dipole moment with field are as expected. For high enough fields, energy levels of opposite parity will shift towards one another. When these levels get close enough in energy, they will avoid crossing, which alters the expected shape of the level.

The Stark perturbation adds a small amount of other states to the original unperturbed wavefunction, which is the mechanism by which a non-zero dipole moment arises, as explained above [50]. Figure 2.4 shows how the mixing of opposite-parity states increases as the electric field increases for an eigenstate which is the $50S_{1/2}$ state at zero field. For the parameters of this experiment, the $50S_{1/2}$ state has a maximum dipole moment of about 200 D at a field of 2 V/cm.

I have now shown that I can produce both a shift in the energy level, and a controllable, induced dipole moment by applying an external electric field. These

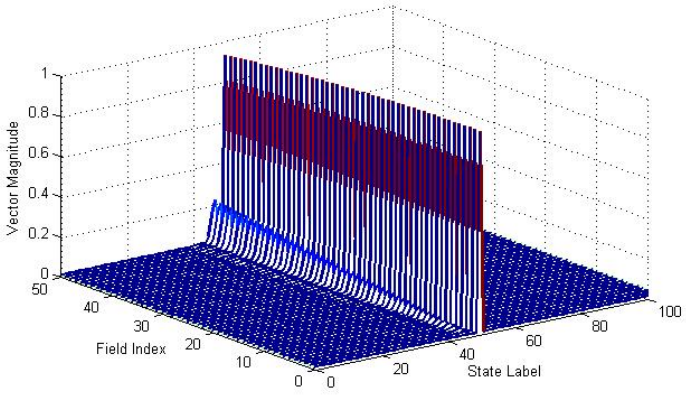

Figure 2.4: A plot of the wavefunction of the $50S_{1/2}$ state as the electric field increases. The sharp peak is the contribution of the unperturbed $50S_{1/2}$ wavefunction, while the smaller peak that increases as the field index increases is an adjacent P-state. The field index is the loop variable used to iterate the increase in the electric field and is approximately equal to 0.1 V/cm for this plot.

tools will be useful in creating a variable-DDI state that can be used for studies of dipolar matter.

2.5 Experimental Implications

In Chapter 1, I discussed the theoretical work done in [12]. In this work, the authors consider increasing the effect of a blockading potential by decreasing the temperature of a cloud. They showed that rather than forming a condensate, the cloud will self-order and form what they call a droplet crystal, in which the atoms pack closely but are separated by clearly-defined density minima between each droplet. By using the Stark shift, I could increase the effect of atom-atom interactions without changing the temperature. In this system, I could see a condensed cloud form a droplet crystal from the superfluid phase, rather than from a thermal cloud. In Chapter 4, I will report how I have begun to implement the Stark shift in an ensemble of thermal atoms with an interparticle spacing on the order of the blockade radius due to the DDI.

Chapter 3

Rydberg-Dressed Atoms

3.1 Overview

There have been numerous theoretical predictions of novel phases of matter in ultracold atomic systems with long-range interactions, including dipolar crystals [46, 40, 42, 11], supersolids, [51, 23, 11], striped and checkerboard phases [51, 23, 36], and others [4]. These calculations have generally assumed the existence of ground-state polar molecules with dipole moments in the range of $2-5ea_0$. Although there have been dramatic accomplishments recently in the production of ground-state polar molecules [23], they have yet to be used for such dipolar many-body physics, and are challenging to produce. Magnetic dipole moments are another promising avenue, with dipole moments similar to those of polar molecules. The magnetic dipole moment of chromium is $3ea_0$ [26]. As has been pointed out in [46], Rydberg atoms might also be able to fill this role. The maximum dipole moment of a Rydberg atom with principal quantum number n is of order n^2ea_0, which is orders of magnitude larger than needed for predicted dipolar effects. In fact this dipole moment is so large that the interparticle forces would overwhelm any optical trapping forces from an optical lattice. In addition, the typical lifetime of a Rydberg state with $n = 50$ is about 100 μs [21], which is too short to allow a many-body system to reach equilibrium. Because the full Rydberg-Rydberg interactions are so

strong, we can use a state with only a fraction of those interactions, something we can achieve by creating a wavefunction that is mostly ground state with a small, adjustable Rydberg component, using a coherent coupling, which dresses the atom [13]. This goal would be accomplished with laser irradiation of ground state atoms on a timescale long compared to the excitation time of the Rydberg state, coherently coupling the ground state to the Rydberg state via a one- or two-photon transition. We can imagine creating atoms that have only 1% Rydberg character, which is still sufficient to create interesting dipolar physics. This amount of Rydberg character increases the lifetimes to $\sim$ 10 ms, which may allow enough time for the system to come to equilibrium. The admixture fraction is controllable by adjusting the coupling laser detuning and intensity, and thus would also give a tunable dipolar coupling between atoms, which could be a useful feature in exploring the effects of long-range interactions. Additionally, the dipole-dipole interaction could be dependent upon an externally-applied static electric field, for exmple one that tunes the atoms near a Förster resonance [60], or induces a dipole moment via the Stark effect [50]. This work represents theoretical calculations done in direct collaboration with my advisor, Dr. Steven Rolston, which was published in [33]. Since the publication of this work, there has been additional interest in the theoretical and experimental implications of creating a Rydberg-dressed state, which will be discussed at the end of this chapter.

In what follows, we will assume an idealized Rydberg coupling laser, described solely by a Rabi frequency Ω and a detuning δ with respect to the one-atom Rydberg transition. In practice this excitation would be created through a two-photon process

with a large intermediate state detuning to assure coherent coupling, with a two-photon Rabi frequency given by

$$\Omega^{(2)} = \frac{\Omega_1 \Omega_2}{2\delta_i} \tag{3.1}$$

for $\delta_i \gg \Gamma_i$, where δ_i and Γ_i are the detuning and linewidth of the intermediate state. In [48] they demonstrate coherent coupling between a ground and Rydberg level in Rb with a two-photon Rabi frequency of $\sim$ 100 kHz, and an intermediate state detuning of $\sim$ 500 MHz. Our goal is to create Rydberg-dressed atoms with a wavefunction

$$|\psi\rangle = \alpha|g\rangle + \beta|r\rangle \tag{3.2}$$

where $|g\rangle$ is the ground state and $|r\rangle$ is the Rydberg state. Such a state would have a spontaneous decay rate of

$$\gamma \sim |\langle g|\vec{d}|\psi\rangle|^2 \sim \beta^2 \gamma_r \tag{3.3}$$

where γ_r is the Rydberg decay rate, and $\vec{d}$ is the dipole operator for spontaneous emission from the Rydberg state [50]. It is tempting to then simply calculate the dipole-dipole interaction between the two dressed states as

$$\epsilon_{int,(naive)} = \langle\psi|U_{dd}|\psi\rangle = \beta^2\langle r|U_{dd}|r\rangle = \beta^2\epsilon_r \tag{3.4}$$

where U_{dd} is the usual dipole-dipole operator between Rydberg states, and ϵ_r is the full interaction energy between two Rydbergs, which can be of order 10 GHz for R = 1 μm and n $\sim$ 50. As we will see below, this expression is in general invalid,

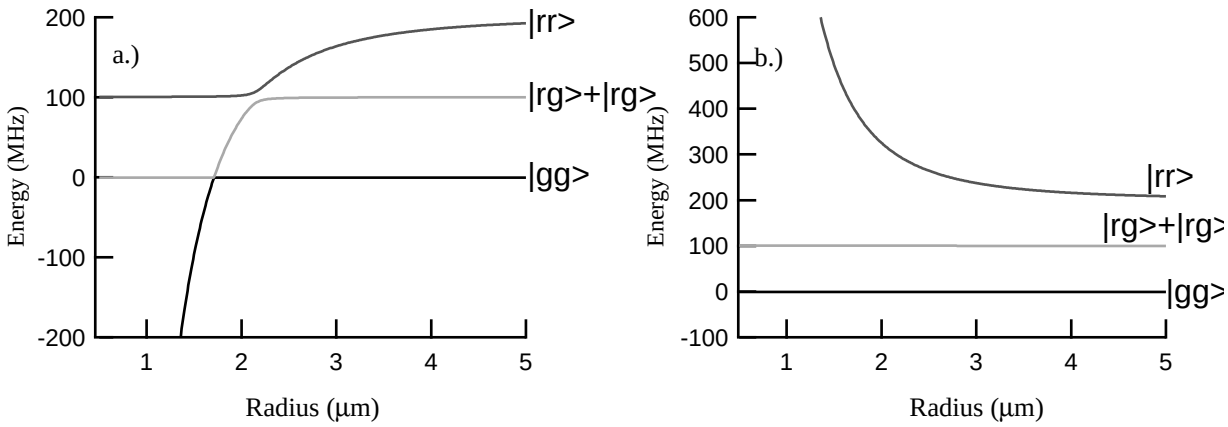

Figure 3.1: The energy levels of the two-atom state for $\Omega/2\pi = 10$ MHz, $\delta/2\pi = 100$ MHz, and a.) $c_3/2\pi = -1000$ MHz$\times\mu m^3$, and b.) $c_3/2\pi = 1000$ MHz$\times\mu m^3$.

because the atom-atom interactions will cause a blockade effect [32, 58, 20], such that the two-atom wavefunction contains much less than β^2 of the $|r\rangle|r\rangle$ state. The correct procedure is to calculate the dressed states for two atoms simultaneously. The blockade effect will arise naturally out of the dressed eigenstates of this two-atom system.

3.2 Two Interacting Dressed Atoms

The simplest case of interacting dressed atoms to consider is the two-atom case. We could write a 4×4 Hamiltonian matrix in the basis $|gg\rangle|N\rangle, |gr\rangle|N+1\rangle, |rg\rangle|N+1\rangle, |rr\rangle|N+2\rangle$, but if instead we use a basis with $1/\sqrt{2}(|gr\rangle \pm |rg\rangle)|N+1\rangle$, the antisymmetric state is uncoupled, and can be ignored. The resulting 3×3 Hamiltonian in the basis $|gg\rangle|N\rangle, 1/\sqrt{2}(|gr\rangle + |rg\rangle)|N+1\rangle, |rr\rangle|N+2\rangle$ can be written

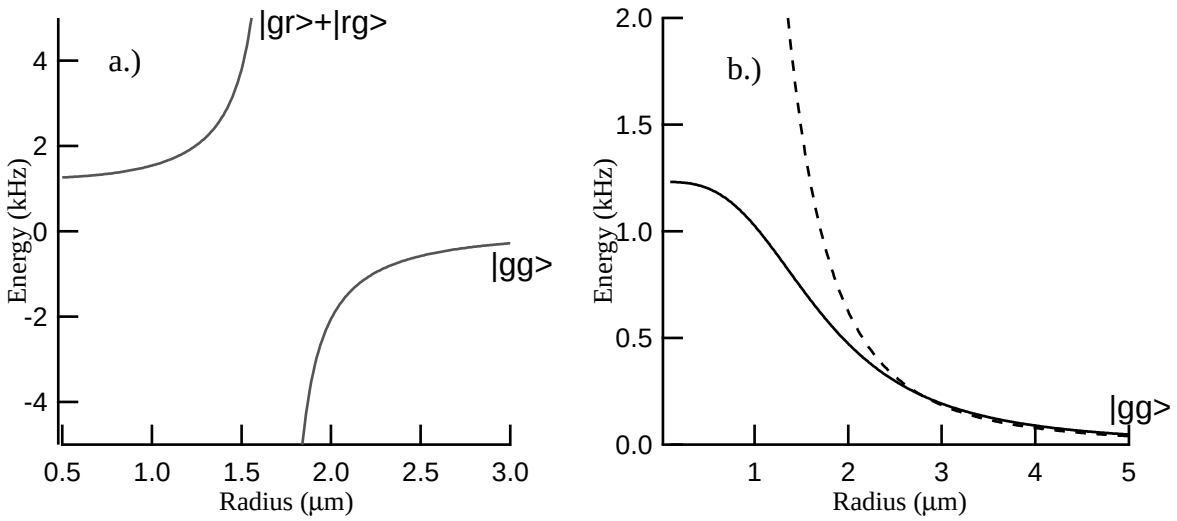

Figure 3.2: A detail of the interaction energies for the same parameters considered in Fig. 3.1, for (a) c_3 <0 and (b) c_3 >0. Panel (b) also shows the convergence with an interaction $\sim 1/r^3$ at longer distances (dashed line).

as

$$H = \hbar \begin{pmatrix} 0 & \frac{\Omega}{\sqrt{2}} & 0 \\ \frac{\Omega}{\sqrt{2}} & \delta & \frac{\Omega}{\sqrt{2}} \\ 0 & \frac{\Omega}{\sqrt{2}} & 2\delta + U_{dd} \end{pmatrix}. \tag{3.5}$$

If $U_{dd} = 0$, we recover the dressed states and eigenenergies for two independent dressed atoms, as expected. We used the two-photon Rabi frequency given in (3.1) for Ω. After diagonalizing the matrix, we find the energy levels as shown in Fig. 3.1, where, for example, we have used a simple c_3/R^3 for the dipole-dipole interaction energy, with $c_3/2\pi = \pm 1$ GHz$\times\mu$m^3, typical for a dipole-dipole interaction for $n \sim 40 - 50$, assuming an applied static electric field. We subtract off the constant light shift due to the coupling laser so that we plot the interaction energy solely due to the two-atom effects (for simplicity, we also ignore the angular dependence of the

dipole interaction, effectively assuming a fixed interatomic axis). Figure 3.1 shows two cases, for positive and negative c_3. In the case of negative c_3 there is an avoided crossing when the laser is two-photon resonant with the dipole-shifted $|rr\rangle$ state, i.e. $2\delta = -c_3/R^3$. We consider both the positive and negative c_3 cases with the detuning chosen so that the interaction energy at short range is positive. Although the DDI is anisotropic in three dimensions, reduced dimensionality experiments, such as those proposed in [47] and [35] give rise to isotropic DDIs which can be isotropically repulsive in two dimensions and attractive in a one-dimensional cloud. Because the trapping potential confines the atomic gas, an attractive interaction would lead to collapse of the cloud rather than emergent order [35]. Figure 3.2 shows a detail of the interaction energies. Note that inside this avoided crossing the eigenenergy of the state that connects to the ground state (the state of interest in the context of a Rydberg dressed atom) is almost independent of R, while outside the crossing it falls off rapidly with R. For positive c_3 (Figs. 3.1b, 3.2b) there is no avoided crossing, yet the eigenenergy also becomes independent of R at distances less than about 0.5 μm, which is comparable to optical lattice spacings. This R-independence is a consequence of the blockade phenomenon. The large U_{dd} term in the Hamiltonian makes the coupling from the single-atom excited state to the doubly excited state off-resonant, significantly reducing the $|rr\rangle$ component of the two-atom wavefunction (to much less than β^2).

3.3 Two-Atom Eigenstates

We can find the eigenstates of this matrix, as a function of R. Examination of these eigenvectors shows that for the eigenvector associated with the lowest energy eigenvalue, the system is predominantly in the ground state, with small amounts of the two excited states mixed in. Using these state populations, we can calculate the percentage of Rydberg in the admixed state from the expression

$$2|\langle rr|\psi\rangle|^2 + \frac{1}{2}|\langle gr|\psi\rangle + \langle rg|\psi\rangle|^2 \tag{3.6}$$

which shows that, for the values used previously, the state is 0.5% in the Rydberg state, which yields a spontaneous emission rate of 40 s^{-1}. Inside the blockade radius, the system cannot be in the state in which both atoms are excited to the Rydberg level, due to blockade, so the Rydberg character inside the blockade radius comes from the eigenstate where only one of the atoms is excited to the Rydberg level.

In the limit when $U_{dd} \gg \delta$, at small R we can expand the ground-state energy of this matrix near $R = 0$. The ground state energy inside the blockade radius becomes $E_{gg}/\hbar \approx (1/2)(\delta - \sqrt{2\Omega^2 + \delta^2})$. Taking the difference between this energy and the non-interacting ground state energy gives an energy due to interactions of $E_{int}/\hbar \sim (1/8)(\Omega^4/\delta^3)$, for $\delta \gg \Omega$. For experiments with cold atoms, interaction energies need to be of the order of kHz, of the same order as ground state atom-atom interactions for atoms trapped in a single lattice site (such as is relevant for the Bose-Hubbard Hamiltonian). From this expression, we can see that it is possible to achieve such a magnitude of interaction energy with Rabi frequencies of order 10 MHz and detunings of order 100 MHz, while at the same time keeping

the Rydberg fraction to 1% or less (necessary for sufficiently small spontaneous emission rates). The Ω^4 dependence of the interaction energy puts a premium on large Rabi frequencies, which will be the primary experimental challenge, especially if it needs to be implemented over a large spatial volume. Recalling the fact that, experimentally, this would be a two-photon Rabi frequency, it would be difficult to have a large Rabi frequency in the regime in which the detuning is large enough that the two-photon population transfer remains coherent.

A second limiting case we can consider is when the atoms are separated by a distance much greater than the blockade radius, or $2\delta \gg U_{dd}$. We find that the ground-state energy eigenvalue dependent on R scales as $U_{dd}(1/16)\Omega^4/\delta^4$. This result is as expected: if we can ignore blockade, the admixture ratio of the excited state for a single atom goes as $\beta \sim (1/2)\Omega/\delta$, so the doubly excited state mixture would go as β^2, and the matrix element $\langle rr|V_{dd}|rr\rangle$ scales with β^4, as found. Note that once again the interaction energy scales as Ω^4.

The above discussions are independent of the actual nature of the atom-atom interaction. Although presented in terms of a pure dipole-dipole interaction, $\sim c_3/R^3$, the same blockade mechanism applies for any interaction larger than the detuning. Figure 3.3 shows the energy of the dressed state connected to the ground state for two interactions : pure dipole-dipole (c_3/R^3) and pure van der Waals (c_6/R^6). A potential such as that shown in [60] for two interacting 50s Rb atoms that is dipolar at short range and van der Waals at long range would fall in between the curves shown in Fig. 3.3. In all cases the eigenenergies evolve similarly with R, with the only difference the rate of change with R.

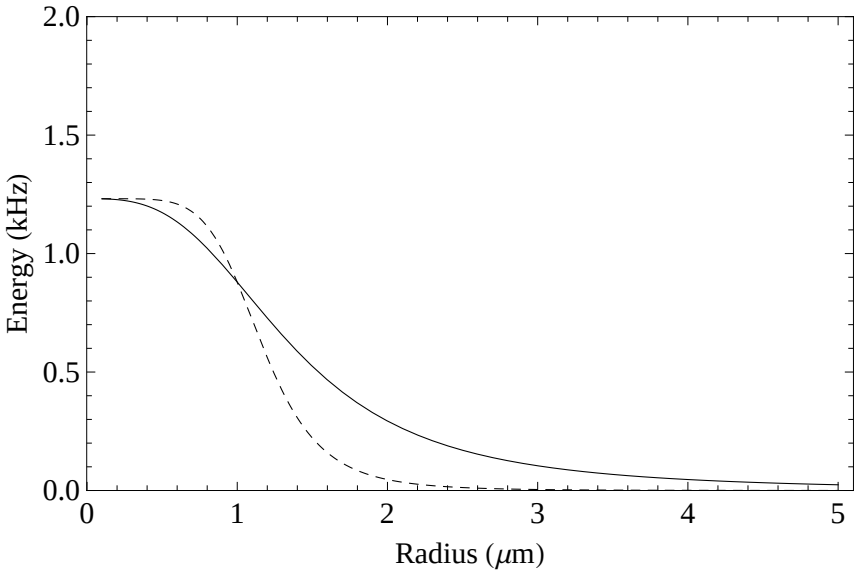

Figure 3.3: The energy of the dressed state, for two different interactions: the dipole-dipole that varies as $1/R^3$ (solid), and the van der Waals that varies as $1/R^6$ (dashed), for $\delta/2\pi = 100$ MHz, $c_3/2\pi = 1000$ MHz$\times\mu m^3$, and $c_6/2\pi = 500$ MHz$\times\mu m^6$.

3.4 Possible Experimental Implications

The R dependence of the interactions shown in Figs. 3.1 and 3.2 is unlike the dipole-dipole $1/R^3$ interaction assumed in most theoretical treatments examining the many-body physics effects of these interactions. It is possible to recover an interaction of this form by working at interatomic distances that are large compared to the critical distance set by the condition where $2\delta = U(R_c)$, but it will be challenging to work in this regime with reasonable parameters. There are a number of requirements: the size of the interaction energy should be sufficiently large, in the 1-10 kHz range (similar to a BEC chemical potential or the atom-atom interaction in a typical lattice) and the spontaneous emission lifetime should be sufficiently long such that the many-body system can come into equilibrium ($\geq$ 10 ms); the relevant interatomic distance should match typical distances, either a lattice spacing or the average interparticle distance in a gas (0.25 - 1 μm). It is difficult to achieve all these requirements for reasonable values of the coupling Rabi frequency. Ref [46] suggests working at rather low principal quantum numbers (n=20), but requires a large Rabi frequency (100 MHz) and yields a short lifetime (5 ms).

Producing standard dipolar physics with Rydberg-dressed atoms seems challenging at best. Another approach is to look at the R-dependent interactions that are possible with accessible experimental parameters and to consider new many-body physics that is not possible for normal condensed matter systems. While such many-body states are beyond the scope of this work, we can speculate. If we consider the simpler case without any level crossings (Fig. 3.3), we have an interaction

that is repulsive and R-independent up to a critical radius, after which it falls off rapidly towards zero. We can consider the impact of this interaction on a gas and on atoms trapped in an optical lattice. If the density was low enough for a gas of atoms, this interaction would look essentially like a contact interaction. At very high densities where the interatomic spacing is small compared to R_c the interactions just provide an overall energy shift, presumably with little impact on the system. In an intermediate density region, however, the cutoff at R_c can be expected to have significant impact on the correlation functions of the gas, perhaps leading to exotic phases and order in the cloud. For an optical lattice, the addition of a nearest neighbor interaction to the Bose-Hubbard model leads to such phenomena as a supersolid phase [51]. With the Rydberg-dressed atom interactions we could have a situation in which the first n-neighbor interactions are the same, followed by little or no interactions. As this situation has no condensed matter analog, prediction is difficult, but novel phases seem likely to exist. Finally, because parameters exist that achieve reasonable interaction strengths and lifetimes with detunings ≤ 1 GHz, we can also consider introducing spin dependence into such interactions. If a two-level spin system is established between two sublevels in the different hyperfine states of an alkali atom such as Rb, we can map all these interactions onto a spin-dependent model, as only one of the levels would interact with the dressing laser.

One important and simplifying assumption we have made with this treatment is ignoring any short range physics, i.e. assuming a single dipolar coupling at small R. This assumption will not be valid when the dipole-dipole shift is on the order of the spacing between neighboring levels, and the energy spectrum becomes extremely

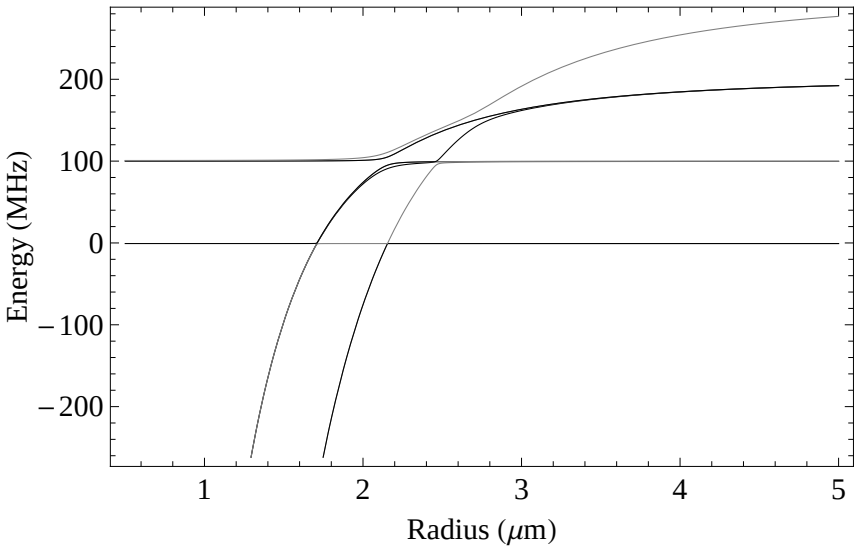

Figure 3.4: The four eigenenergy levels of the three-atom system in the two-dimensional configuration for $\Omega/2\pi = 10$ MHz, $\delta/2\pi = 100$ MHz, and $c_3/2\pi = -1000$ MHz$\times\mu m^3$.

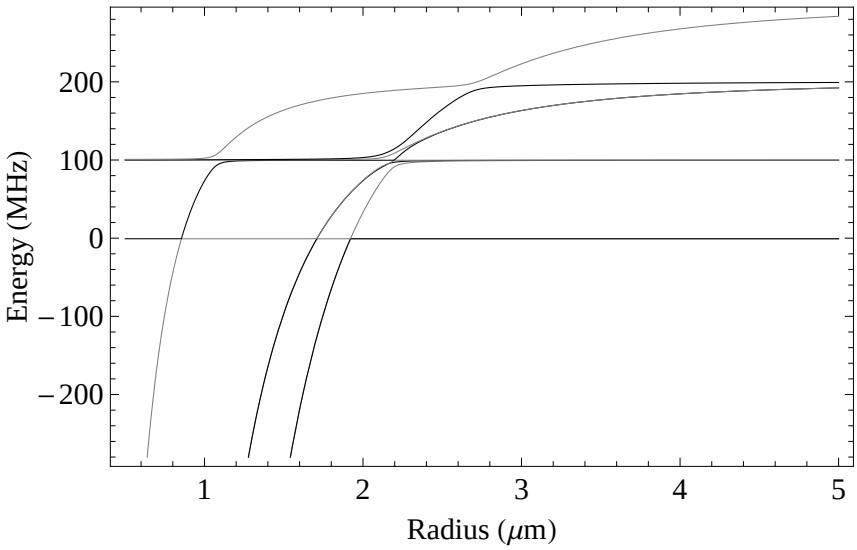

Figure 3.5: The eight eigenenergy levels of the three-atom system in the one-dimensional configuration for $\Omega/2\pi = 10$ MHz, $\delta/2\pi = 100$ MHz, and $c_3/2\pi = -1000$ MHz$\times\mu m^3$.

crowded and complicated at short range (see [52] for example). More detailed calculations beyond simple dispersion expansions of the dipole coupling are needed to understand the energy spectrum as well as potential loss mechanisms. The effect of the dressing at short distance may be more robust than it seems, however, because it depends solely on the blockade effect. As long as the interactions dominate the detuning their actual value is irrelevant. Of course if the coupling laser couples directly to a short-range molecular state, potentially large losses would ensue.

3.5 Three Interacting Dressed Atoms

So far, we have examined only the simplest interacting system: two interacting dressed atoms. In order to extend these calculations to many-body systems in the future, it is necessary to explore a more complicated system of atoms. The next level of complextiy would be a system of three interacting dressed atoms. We can examine the eigenvalues for a system of three dressed atoms, where the Hamiltonian has multiple independent interaction terms on the diagonal, in two simple configurations: a one-dimensional configuration that examines next-nearest neighbor interactions, and a two-dimensional configuration. The one-dimensional configuration is a line of the three atoms, with distance R between adjacent atoms, and the two-dimensional configuration is each atom on the vertex of an equilateral triangle with side R.

The Hamiltonian of atoms arranged in the two-dimensional configuration has two independent diagonal terms. Because the atoms are equidistant, the diagonal terms for each amount of excitation are degenerate and we can reduce the 8×8 matrix to a 4×4 matrix

$$H = \hbar \begin{pmatrix} 0 & \frac{\Omega}{\sqrt{2}} & 0 & 0 \\ \frac{\Omega}{\sqrt{2}} & \delta & \sqrt{\frac{3}{2}}\Omega & 0 \\ 0 & \sqrt{\frac{3}{2}}\Omega & 2\delta + \frac{c_3}{R^3} & \Omega \\ 0 & 0 & \Omega & 3\delta + 3\frac{c_3}{R^3} \end{pmatrix} \tag{3.7}$$

using the basis: $|ggg\rangle, 1/\sqrt{3}(|rgg\rangle + |grg\rangle + |ggr\rangle, 1/\sqrt{3}(|rrg\rangle + |grr\rangle + |rgr\rangle, and |rrr\rangle$. In this case, there are avoided crossings for $2\delta = -c_3/R^3$, as well as for $3\delta = -3c_3/R^3$

for negative detunings and attractive interactions. For a given detuning, the second of these crossings occurs at a larger interparticle spacing, and is a narrower avoided crossing. This behavior means that the larger interaction occurs at the first, closer, radius. Figure 3.4 shows the energy levels of this system. For negative c_3, the interaction energy looks similar to the two-atom case, with an enhanced value for the same Rabi frequency and detuning.

In the one-dimensional case, in which the three atoms lie on a line, we find an additional avoided crossing, where $2\delta = -c_3/(8R^3)$. This crossing is at an even closer radius, and is wider than the other two. Figure 3.5 shows these avoided crossings as part of the energy level plot. In this reduced-dimension case, we see additional avoided crossings due to the broken degeneracy of some diagonal terms due to the addition of a next nearest neighbor, requiring the full 8×8 matrix for evaluation. Further expanding these calculations to consider a system of four atoms leads only to additional avoided crossings at longer ranges in the energy spectrum. Additionally, the three distinct avoided crossings, where the interaction energy goes from being zero to being large, suggests that one could design states in an optical lattice in which nearest-neighbor atoms have negligible interactions and act as "spectators" to non-nearest-neighbor atoms that interact with a large energy. This follows if one considers an experiment in which the lattice spacing, a, is equal to $r_{crossing}/\sqrt{2}$, so that the nearest neighbors are far from an avoided crossing, and therefore have an interaction energy close to zero, while the next-nearest-neighboring atoms have a separation of $a\sqrt{2}$, or $r_{crossing}$, and experience the large interaction due to the avoided crossing. In the case presented in Fig. 3.5, this situation would correspond

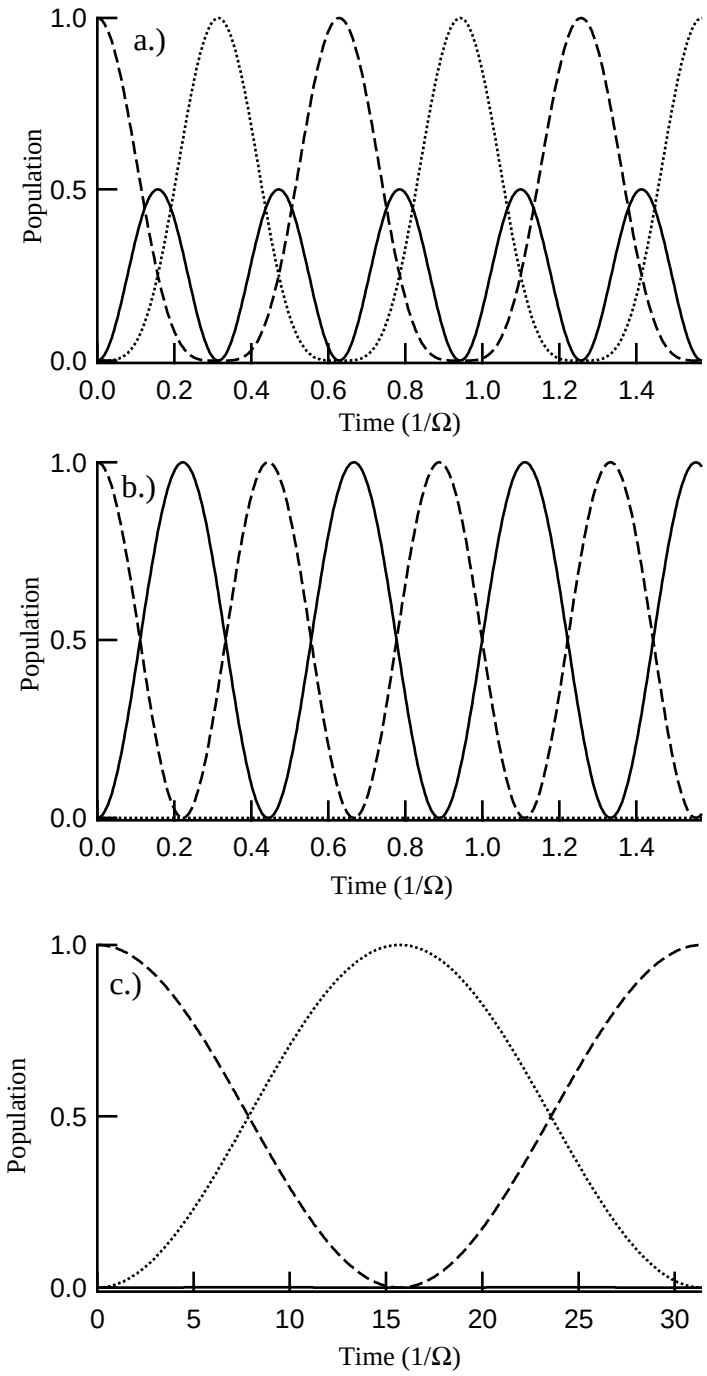

Figure 3.6: The time-dependent evolution of the three eigenstates for atoms separated by 1 μm for a.) $c_3 = 0$, b.) $c_3 \neq 0$, and $\delta = 0$, and c.) $c_3/R^3 = 2\delta$. The curves show the evolution of the states $|gg\rangle$(dashed), $1/\sqrt{2}(|gr\rangle + |rg\rangle)$(solid), and $|rr\rangle$(dotted).

to a lattice spacing of, for example, 1.2 μm.

3.6 Time-Dependent Effects

Although up until this point we have been concerned with the steady-state dressed atoms, since we have expressions for the eigenvalues, it is simple to calculate the time dependence for a sudden turn-on of the laser fields. This calculation can be done by projecting the ground state of the bare atom onto the dressed atom basis, evolving the dressed-atom states in time with the phase factor $\exp(-i\epsilon_i t)$, where ϵ_i is the interaction energy, and then projecting back to the bare-atom basis. Figure 3.6 shows three cases: the evolution of the states $|gg\rangle$, $1/\sqrt{2}(|gr\rangle + |rg\rangle)$, and $|rr\rangle$ for a) no atom-atom interactions, b) atom-atom interactions with $\delta = 0$ (single-atom resonance), and c) atom-atom interactions on the two-atom resonance ($2\delta = U(R)$). For case a) we see Rabi flopping of two independent atoms, with all the population in $|rr\rangle$ for a π-pulse, and population in all three two-atom states during the rest of the evolution. For case b) the blockade effect is apparent, in that there is no observable excitation of the doubly excited state, and the system Rabi flops between $|gg\rangle$ and $|gr\rangle + |rg\rangle$. For case c) there is no population of single Rydberg atoms and the system flops between $|gg\rangle$ and $|rr\rangle$. Note that the flopping time scale is longer, because this is a two-photon coupling with a correspondingly smaller Rabi frequency.

As can be seen in the figure, using a $\pi/2$-pulse with respect to the two-photon Rabi frequency should be a simple way to create an entangled state, $|gg\rangle + |rr\rangle$. Only

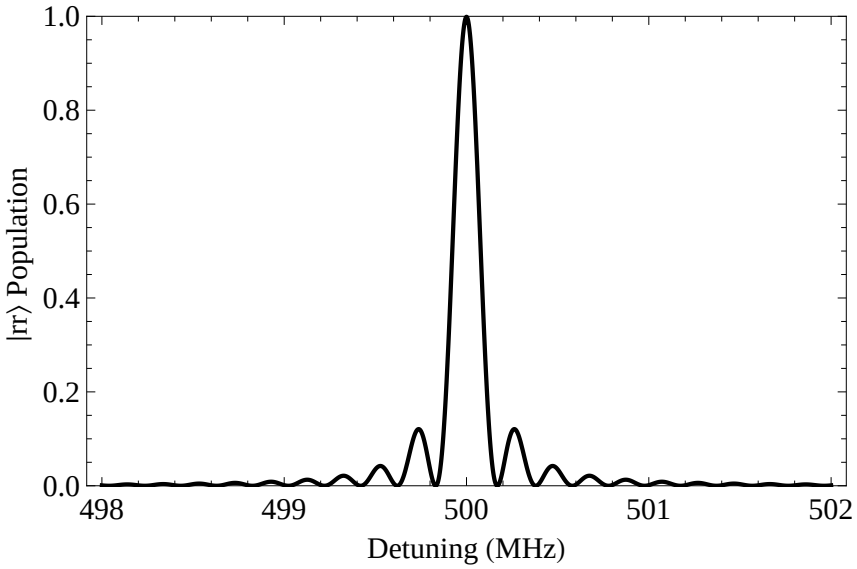

Figure 3.7: The population of the doubly-excited state after a pulse of duration $t = 16/\Omega$ at different detunings.

atom pairs that are at the correct distance to be two-photon resonant will Rabi flop, allowing for the creation of entanglement of pairs of atoms that are separated by the distance for which the two-photon effect is resonant, with non-entangled ground state atoms at intermediate separations. Figure 3.7 shows the population at the end of a pulse of duration $t = 16/\Omega$ as a function of the detuning. For small detunings the blockade is evident as there is practically no population of the state $|rr\rangle$. At the two-photon resonance condition, all of the population can get excited into $|rr\rangle$ for the appropriate pulse duration. As mentioned in Chapter 1, this experiment would require a fixed internuclear separation, and would only be possible in an optical lattice system rather than an atomic gas.

3.7 Summary of Original Calculation

In summary we have considered creating Rydberg-dressed atoms, with small admixtures of Rydberg character, to study dipolar many-body physics. We find that the blockade phenomena prevents large interaction energies at small distances, set by a critical radius at which the detuning is equal to the dipolar interaction energy. The resulting R-dependent interaction energy can have sufficient size to be relevant for many-body physics of cold atoms, but its functional form is fundamentally different from the $1/R^3$ dipolar interaction that one expects. Instead the energy tends to a constant value at small R with a crossover to $1/R^3$ at the critical distance. This form is unlike any interactions in condensed matter physics and may open up the possibility of novel many-body states. While these calculations point to experimental parameters that are challenging to achieve, in the future we hope to implement an experiment based on these calculations. A recent paper, [43], discusses further many-body effects of the interactions of dressed Rydberg atoms.

3.8 Self-Trapping of Rydberg-Dressed Atoms in a BEC

Since the publication of the above work [33], there has been increased interest in the implications of using Rydberg-dressed atoms in cold-atom experiments. In [39], the authors consider a system where the Rydberg atoms interact primarily via the van der Waals interaction. Because this interaction scales as n^{11}, this interaction, while shorter-range than the dipole-dipole interaction, can be much stronger than those between ground-state atoms. Additionally, because the interaction does

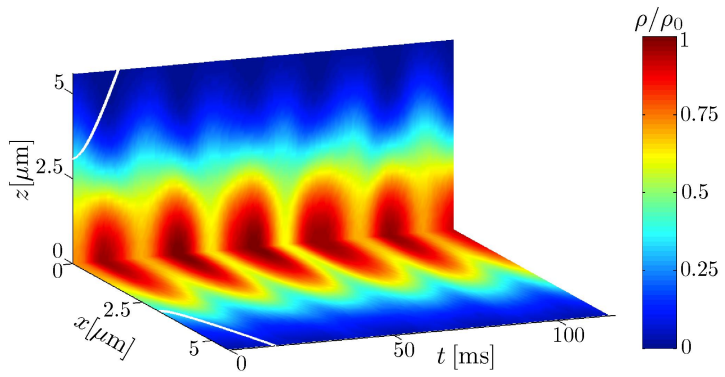

Figure 3.8: The free expansion of the self-trapped BEC of Rydberg-dressed atoms. The white line shows the expansion of an undressed cloud. From [39].

not depend on parity-breaking to arise, there is no need for Förster resonances or external fields to achieve the maximum interaction between the full Rydberg atoms.

In [39], the authors consider states for which the c_6 term of the van der Waals interaction is attractive, which for ^{87}Rb means working with the D-state. The authors then show that the potential of these Rydberg-dressed atoms describes soliton formation. By simulating this potential in an ensemble of atoms with densities comparable to a BEC, the authors show that the weak attractive interaction between the atoms provides self-trapping of the cloud as it undergoes free expansion. Figure 3.8 shows how the expansion of a Rydberg-dressed condensate compares with the expansion of an undressed cloud. The false-color image shows the number density at different spatial positions for several different times of flight after release from the trap. The comparison with the white lines, which show the width of a freely-

expanding undressed condenstate, shows that the dressed cloud exhibits behavior consistent with remaining trapped in some way despite the removal of magnetic or optical confinement.

[39] also suggests a mechanism that we could explore in our own experiment. Because the DDI is anisotropic, it might be possible to observe this self-trapping in the attractive direction of the DDI. This is a possible signature of the achievement of proper Rydberg dressing without directly measuring the full Rydberg excitation. Because too strong of an attractive interaction would cause collapse of the cloud, it is possible to use this self-trapping as a way to calibrate the fraction of the dressed state that is in the Rydberg state.

Chapter 4

Experimental Apparatus

4.1 Overview

We explored the Rydberg blockade effect in an external static electric field in a magneto-optical trap (MOT) of ^{87}Rb atoms at low temperatures. Because the density of a MOT is $\sim 1\mu\text{m}^{-3}$, it was possible to study the continuous variation of the excitation rate as we increased the dipole moment induced by the external field. This density is high enough that we see blockade as we increase the induced dipole moment, but not so high that the cloud is blockaded by zero-field interactions, as discussed in Chapters 5 and 6. For future studies, we plan to work in a Bose-Einstein condensation (BEC) in an optical lattice. This Chapter reports on work done in collaboration with other graduate students in the lab. Further details of their contributions can be found in [2, 17, 6].

The excitation scheme to produce Rydberg atoms with $n \sim 50$ or greater is a two-photon transition, with one photon provided by the MOT trapping lasers, and the other photon produced by frequency doubling a 960-nm diode laser.

4.2 Atom Traps

4.2.1 Magneto-Optical Trap

The primary trap used in this research was a magneto-optical trap (MOT) of ^{87}Rb atoms. The MOT can trap up to 10^9 atoms, with a temperature of <1 mK, and a density of about 1 μm^{-3}. The MOT is produced by superimposing a magnetic quadrupole trap over an optical molasses to slow incoming atoms and confine them in three dimensions [6, 17].

The magnetic quadrupole trap is formed by running ∼45 A of current through a U-shaped wire that sits in-vacuum towards the top of our chamber. The field from this wire creates a field gradient, which is adjusted to form a trap zero by means of bias coils in all three dimensions, which sit outside the chamber. The external coils and the U-shaped wire are water-cooled to prevent overheating due to the large currents passing through them. Additionally, all the wires are connected to insulated gate bipolar transistors (IGBT) to provide fast switching when we wish to turn the field off. By using the IGBTs, we can turn the fields off on the timescale of a few μs.

We create the optical molasses with four beams. Two beams counter propagate through side windows of the chamber, parallel to the plane of the optical table. We create confinement in the other two directions by sending two beams in at an angle through the bottom window of the chamber. Also in-vacuum, sitting just below the U-shaped wire is a gold mirror, which retroreflects these beams, forming a three-dimensional MOT.

We trap atoms in the MOT by initially slowing a hot Rb vapor. We send the vapor into a collimator and through a Zeeman slower [44]. The slower that we use is about 0.5 m long. The atoms slow from 100 °C to speeds slow enough to be captured in the MOT, which corresponds to slowing from about 200 m/s to about 20 cm/s. Our four-beam setup has a smaller capture region than traditional six-beam setups, but we can still load 10^9 atoms into our MOT in about 5-10 s.

In order to create the cloud size we need for the experiment described in the next chapter, we reduce the number of atoms in the MOT. We require a small MOT to ensure that the size of the MOT does not extend beyond the size of our Rydberg excitation beam. In order to reduce the size of the MOT, we detune the slower by >20 MHz from its optimal value, so that we load fewer atoms. We can also reduce the loading time to further reduce the MOT number.

From the MOT, we can load the atoms into an Ioffe-Pritchard magnetic trap, formed by an in-vacuum Z-shaped wire combined with external bias coils. In the magnetic trap, we can use RF evaporation to cool the cloud further. We have observed Bose-Einstein condensation in this trap [17]. With a condensed cloud, or a near-condensed cloud, we can load the atoms into an optical lattice for further studies.

4.2.2 Optical Lattice

The design of our MOT provides for the possibility of creating a phase-locked one-dimensional optical lattice with little adjustment. The mirror above the atoms

can be used to retroreflect a beam entering through the bottom of the chamber. When a beam is applied directly vertically through the bottom window of the chamber, it creates a standing wave of light, forming a lattice potential with a separation of $\lambda/2$. We use a Tekhnoscan Ti:Sapph laser, which can be scanned over a range of wavelengths. On average, we use a wavelength of 800 nm, which creates a lattice spacing of 400 nm. Because the forward-propagating and counter-propagating lattice beams both reflect off the same mirror surface, they are phase-locked.

In order to create the two-dimensional systems proposed in the previous literature we could use a one-dimensional optical lattice to divide the atom cloud into a series of two-dimensional traps, or pancakes. The design of our lattice beams and the generation of the electric field provides a setup similar to that proposed in [47]. The electric field applied vertically would align the dipole moments of the Rydberg atoms perpendicularly to the two-dimensional ensembles created by the lattice beams running parallel to the electric field.

This experiment could be extended easily to explore the effects of DDIs in two-dimensional systems. A first step would be to create a three-dimensional cloud of Rydberg-dressed atoms with their dipole moments aligned vertically, to see if we can see an effect on the free expansion of the cloud as we increase the interactions. As mentioned in the previous chapter, we could change these interactions for a given interparticle spacing by changing the detuning and power of the dressing beam. Another method by which we can affect the dipole moment is by changing the magnitude of the externally-applied electric field, which we have demonstrated and will be discussed in the next chapter.

4.2.3 Dipole Trap

Our setup has the capability to trap atoms in a moving optical dipole trap. This trapping allows us to move the atoms from the main chamber, in which we can magnetically trap and evaporatively cool the atoms, into a smaller peripheral chamber in which we can detect Rydberg atoms via field ionization and ion detection with a microchannel plate (MCP) The dipole trap is formed by focusing a 15-W Er-doped fiber laser at a wavelength of 1550 nm to a 40-μm-waist spot, forming a region of high intensity. Because the fiber laser is tuned red of the the D-lines in ^{87}Rb, the atoms will be attracted to this region of highest intensity. The dipole trap has been demonstrated in the main chamber, and has been shown to be useful for moving cold atoms over a distance of $\sim$30 cm [6] in our apparatus.

We can move the atoms in the dipole trap by moving the focus of the beam with a lens on an air-bearing stage. As we move the lens on the stage via computer control, the position of the focus changes. The atoms follow the focus of the laser. By altering the relay imaging optics, we can image the waist of the beam through a different window of the chamber, so that the moving lens would pull the atoms from the main chamber into the peripheral chamber with the MCP.

4.3 Rydberg Excitation

We excite Rydberg atoms via a two-photon excitation. We first excite the ground-state $5S_{1/2}$ atoms to the $5P_{3/2}$ state using the 780-nm light that we also use to trap atoms in the MOT. For the data analyzed in this thesis, the first excitation

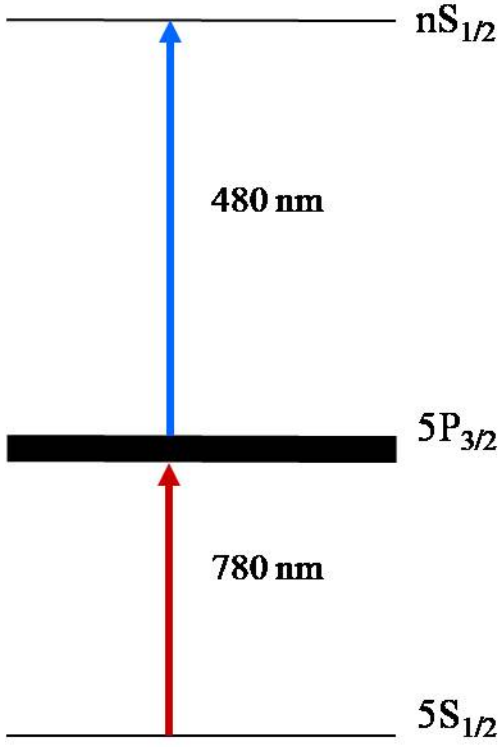

Figure 4.1: Two-photon excitation scheme for Rb Rydbergs: The 780-nm photon also serves as the MOT trapping light, exciting the D_2 transition in ^{87}Rb. The 480-nm photon excites from the $5P_{3/2}$ state to a high-lying Rydberg S state.

is made by the MOT beams themselves and is tuned about 30 MHz to the red of the resonance. The linewidth of this transition is about 6 MHz [56].

We perform a two-photon excitation as shown in Figure 4.1. From the $5P_{3/2}$ state, we can excite to the Rydberg state with a 480-nm photon. Because the spacing of the Rydberg levels is small, we can excite to either an nS state or an nD state. For these experiments, we choose to excite to the $nS_{1/2}$ states to avoid the confusion of having multiple j states within a small frequency range. The frequency differences between adjacent l and n states are easily resolved by the use of a wavemeter with

30-MHz precision.

We have several reasons for choosing a two-photon excitation scheme to produce Rydberg atoms. The data we collected focused on the S angular momentum state in Rb. Because the ^{87}Rb ground state is an S state, it is electric dipole forbidden to excite a Rydberg S state directly from the ground state in a single-photon excitation.

Additionally, the dipole matrix element between the ground state and the Rydberg state is very small, resulting in a low excitation cross-section and the need for more laser power to excite the transition. By considering instead the overlap between the first excited state and the Rydberg states, we can increase our excitation cross-section. An approximation of the Rydberg excitation cross section is given in [21] as

$$\sigma(n) = \frac{\sigma_{PI}}{\Delta W n^3}, \tag{4.1}$$

where σ_{PI} is the photoionization cross-section and ΔW is the energy resolution of the experiment, in our case the linewidth of our laser, which is much larger than the $\sim 7-$kHz natural linewidth of the Rydberg transition. Given an excitation to the same Rydberg n with the same experimental resolution, the Rydberg excitation cross-section will scale with the photoionization cross-section. The rubidium photoionization cross section from the $5S_{1/2}$ state is 1.7×10^{-20} cm^2 [38], while the cross-section from the $5P_{3/2}$ state is $\sim 1 \times 10^{-17}$ cm^2 [16, 19]. Even considering that only about half of our atoms are in the $5P_{3/2}$ in our MOT steady state, the

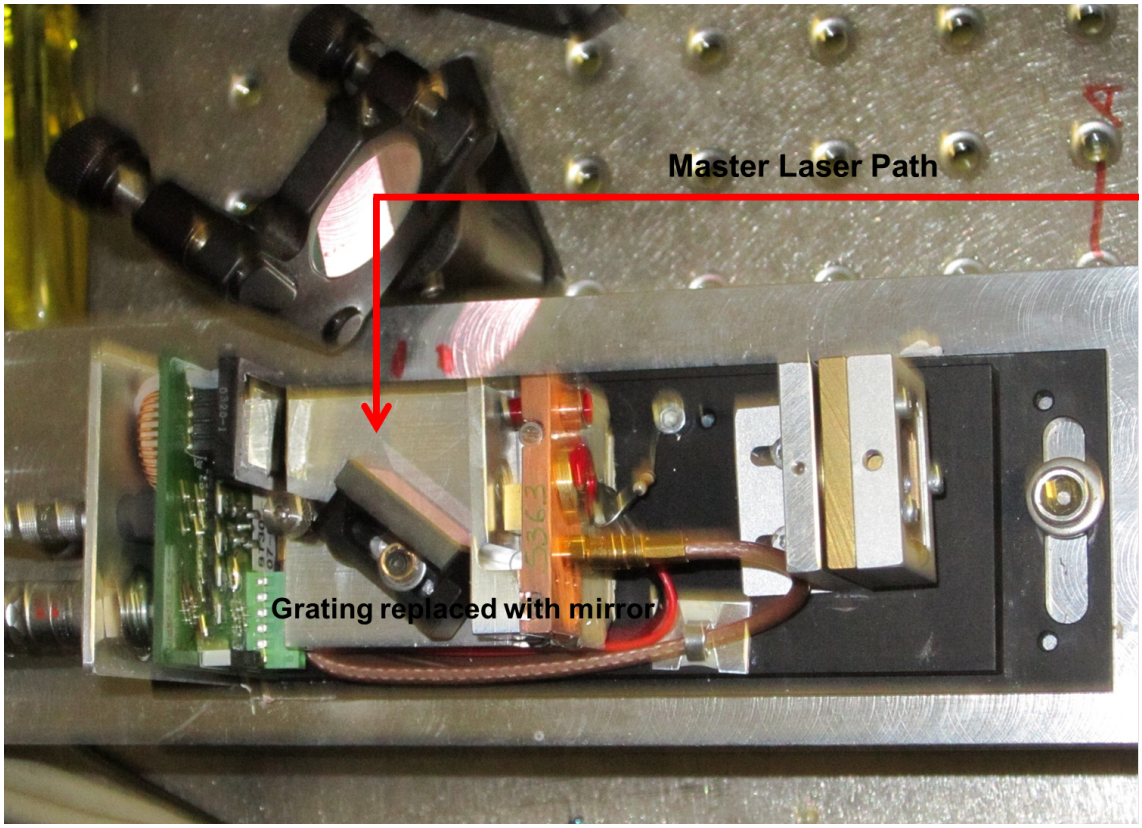

Figure 4.2: The interior of the Sacher tapered amplifier. The injected light path is shown. The labeled mirror replaces the original laser's grating so that we run the diode as an amplifier.

two-photon transition has a cross-section several orders of magnitude greater than the single-photon transition.

4.4 Blue Light Generation

We generate 480-nm light to excite the atoms from the $5P_{3/2}$ state to the $nS_{1/2}$ state by frequency doubling a stable 960-nm diode laser. The details of the blue light stabilization are explained in Appendix A. We inject the light from a home-built 960-nm external cavity diode laser into a Sacher Lasertechnik TEC-300

laser operated as a tapered amplifier, as shown in Figure 4.2. Our master laser diode is a QPhotonics single-mode free-space laser diode with a wavelength range of 950-970 nm and a maximum output power of 100 mW. We place this diode in an external cavity to select the wavelength of about 960 nm and can get about 45 mW of power from this setup. After amplification, we achieve about 500 mW of power out of the tapered amplifier. Before taking the data at 41S, 56S, and 61S, as reported in Chapter 6, I had to replace the TA diode with a Sacher Lasertechnik diode optimized for operation as a TA, with a maximum power of $\sim$1700 mW of power.

As discussed in Chapter 1, the Rydberg linewidth sets the blockade criterion in theory. In practice, the laser linewidth will dominate over the narrow Rydberg linewidth, so we must ensure that our laser linewidth is as narrow as possible. We use the method of self-homodyne spectroscopy to measure our laser linewidths and have found that we can achieve a linewidth of $<$500 kHz for the system described above. Details of this calculation are discussed in Appendix A.

Part of this light is split off to make the signal to which we lock the frequency of the laser. The rest is sent through a system of optics to mode-match the beam with a bow-tie cavity that makes up our frequency doubling system. We use a commercial SpectraPhysics Wavetrain doubler with a lithium triborate crystal. The power at the input of the cavity is just under 60% of the power generated by the TA and we can get a maximum 30 mW of blue light from the doubler. The crystal is primarily phase-matched by angle, though we keep the crystal at a temperature of 35-40 °C.

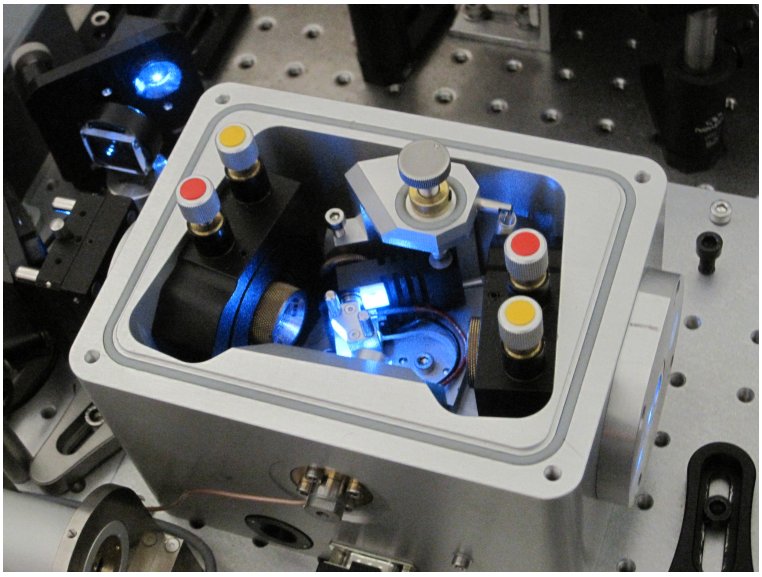

Figure 4.3: The frequency doubling cavity

4.5 Accessing Different Principal Quantum Numbers

We generate our 960-nm pumping light by amplifying a home-built external-cavity diode laser, as described in Appendix A. In order to excite the atom from the $5P_{3/2}$ state to the Rydberg states, we have to ensure that the laser is tuned near a Rydberg resonance. We do this by calculating the necessary wavenumber, as described in [21], and comparing it to the value that we read by analyzing the 960-nm light with a Burleigh wavemeter. We can see the Rydberg signal by observing an increased decay of the MOT as we change the frequency with both coarse and fine adjustment. This increased decay is caused by the high likelihood of background black body radiation ionizing the Rydberg atoms, which are close in energy to the continuum. I will discuss this process in more detail in Chapter 5.

Because the energy spacing between Rydberg levels vary from n to $n+1$ by approximately 1 cm^{-1} around $n = 50$, in order to access ns that are more than a

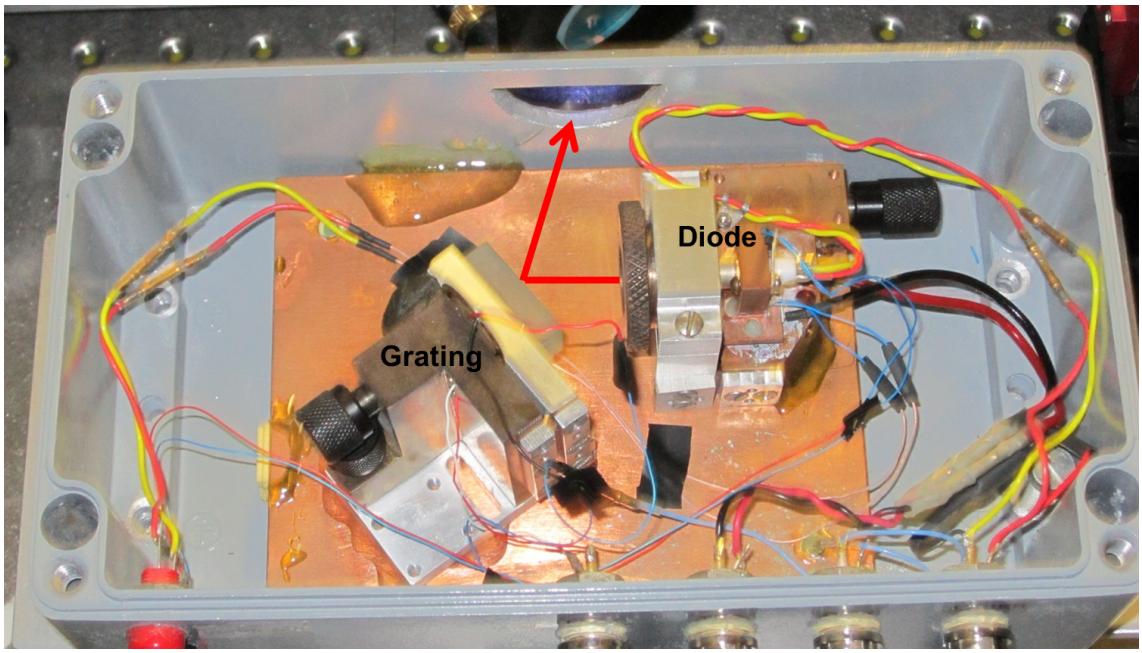

Figure 4.4: The interior of the home-built laser. The grating and diode are labeled and the red line shows the path of the light as it exits the laser case. The grating and diode sit on a large, temperature-controlled copper block.

few integers apart, we must adjust the internal feedback grating in the laser case itself, shown in Figure 4.4. I present a table of Rydberg transition wavenumbers in Appendix B, as I used them to tune the laser near the Rydberg resonance.

4.6 External Static Electric Field

In order to control our Rydberg atoms' dipole moments, we apply an external static electric field. This field also serves to align the dipoles in a single direction, which is necessary to perform the experiments proposed in [47]. As discussed in the previous section, we generate four of the six beams needed to form the optical molasses for our MOT by retroreflecting two beams off an in-vacuum gold mirror that sits in the chamber above the atoms. Because the atoms sit within 1-2 mm of this mirror, this mirror can be used to create a roughly homogeneous, vertical electric field.

We apply voltage, which varies from 0-125V, to two in-vacuum electrodes, which sit on either side of the mirror, as shown in Figure 4.5. These electrodes were originally connected to draw current and were run as rubidium dispensers to load the MOT [17]. We have since abandoned this atomic source, but the electrodes do not impede the paths of any laser beams. Because the gold mirror is grounded, the electric field at the mirror surface is perpendicular, as shown in Fig. 4.6. Because the atoms sit very close to the mirror, we can approximate the mirror as an infinite conducting plane and consider the electric field to be homogeneous and perpendicular across the size of the MOT. According to SimION calculations, which I discuss

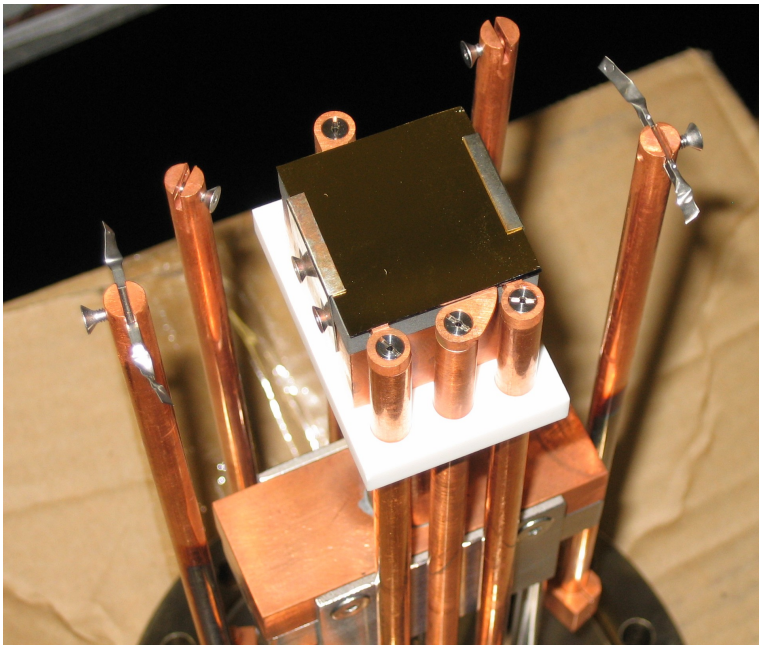

Figure 4.5: The in-vacuum electrodes. This assembly sits upside-down in the vacuum chamber, where the gold mirror retroreflects the MOT beams entering from the bottom of the chamber. The strips of metal on either side of the gold mirror are connected to a voltage supply to create the electric field at the atoms.

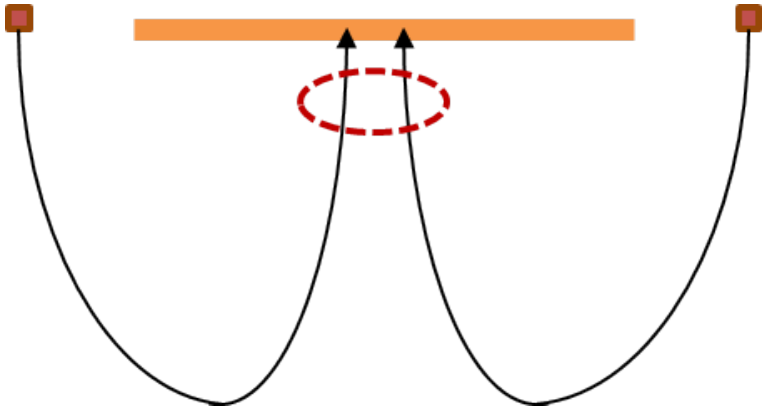

Figure 4.6: A schematic of how the electrodes produce field. The voltage applied to the electrodes (red squares) produces a field (black arrows) that goes perpendicularly into the gold mirror (orange). The red dashed line shows approximately where the atom cloud is produced.

in Appendix B, we have a <2% variation in the field magnitude across of the size of the MOT.

4.7 Current Experimental Operation

This chapter describes some of the experimental tools that we use in the lab to acquire the data presented in Chapters 5 and 6, as well as tools we have designed and tested, but that have not yet been incorporated into the experiment for the sake of collecting the current data. Our present experimental procedure is as follows.

First, we must make sure the blue light is at a wavenumber near that required to excite the $5P_{3/2} \rightarrow nS_{1/2}$ transition. This procedure may require rotation of the grating in the home-built master laser. We then check that the laser is aligned into the doubler cavity and that the laser locks are working. Once we can lock the blue

light near the Rydberg transition, we can use it to illuminate the MOT.

We then form a MOT of ^{87}Rb, using the detuning of the Zeeman slower laser to change the MOT number so that the atom cloud width does not exceed the diameter of the blue beam. We load the MOT for several seconds, and then turn off the loading and hold the MOT while we illuminate it with the blue beam. We apply voltage to the electrodes during the blue-light illumination. After the blue illumination, we image the cloud with absorption imaging, which destroys the cloud.

We do not currently use the dipole trap to move the cloud, nor do we load the atoms into an optical lattice. These tools have been demonstrated in our lab in general, and may be incorporated into this experiment in the future, in order to study further effects of long-range interactions in cold atomic systems.

Chapter 5

Field-Tuned Dipole Blockade

5.1 Overview

While Rydberg blockade has been studied previously, both in the absence of an external field [58, 20], and in the presence of an external field [59], our experiment provides several unique features. First, the detection scheme and setup are designed to be able to excite and observe Rydberg atoms continuously, rather than in a pulsed set up. The times during which I illuminate the atoms with excitation light are much longer than those in previous experiments. This feature makes the following experiment a further step in the direction of producing a Rydberg-dressed state, as the Rydberg-dressed state depends upon the continuous irradiation of the atom with the Rydberg excitation light.

I have observed a controllable interaction between Rydberg atoms in an external electric field by observing the blockade of the Rydberg excitation as a function of the strength of the field. As I increase an external, static field, I see fewer Rydberg atoms produced in the system. My calculations of the induced dipole moment due to the Stark effect in Rydberg atoms suggest that this excitation suppression is due to the DDI between induced dipoles.

I can analyze these data using two methods: a simple analytical model and a Monte-Carlo simulation that models the simplest picture of dipole blockade. I

simulate the excitation and decay of the atoms to and from the Rydberg state in a system of randomly-positioned atoms at the density of our MOT, and then add the condition that atoms interacting with a strong enough DDI are prevented from being excited. This simulation shows that the excitation suppression can be explained by a simple model of dipole blockade and suggests that I have observed a blockade effect that can be tuned with an external field.

5.2 Rydberg Detection

For this experiment, I detect Rydberg excitations by measuring the atoms lost from the MOT. Because Rydberg atoms are near the ionization limit, they have a high likelihood of being spontaneously ionized by the ambient black-body radiation in the lab. Because the decay rate of the MOT (due to background gass collisions) without Rydberg excitation is several orders of magnitude slower than the loss rate with Rydberg excitation, I assume that the primary loss mechanism is black-body ionization. This photoionization rate is fast enough that Rydberg atoms that do not ionize are lost either to transitions to nearby Rydberg states, which I will discuss later in this chapter, or to decay to the MOT-trapped states. For this reason, I assume that any atoms lost from the MOT are in a Rydberg state. The black-body photoionization rate of the $50S_{1/2}$ Rydberg atoms is explored theoretically in detail in [7], and I considered it to be $\sim 100\ s^{-1}$, though this will depend somewhat on the number of Rydbergs excited.

I observe an Autler-Townes spectrum of the Rydberg atoms by sweeping the

frequency of the blue laser. The Autler-Townes effect is an AC Stark effect that occurs when an atom interacts with an oscillating electric field, such as that of a laser field, in a two-photon excitation. This effect causes the spectrum to split up into two peaks, corresponding to the cases where the lasers are on two-photon resonance and where one laser is detuned from the intermediate state, but the second laser is on resonance between the intermediate and final states [5]. Because I measure the spectrum from the MOT loss, the Autler-Townes peaks manifest as drops in the MOT number. Figure 5.1 shows this experimental spectrum that is fit to a curve with the functional form

$$N(f) = N_0 + \frac{A_1}{(f - f_1)^2 + B_1} + \frac{A_2}{(f - f_2)^2 + B_2}, \tag{5.1}$$

which describes a spectrum fit to two Lorentzian peaks. The variables N_0, A_i, B_i, and f_i are adjusted to optimize the fit; in this case, the amplitudes A_i would be <0. I assume this functional form as it keeps the key features of the Autler-Townes doublet and merges to a single Lorentzian function when the two peaks fall at the same frequency, as observed in [24]. The larger peak occurs when the blue laser is on two-photon resonance with the Rydberg level, while the smaller peak occurs when the blue laser is on single-photon resonance with the transition from the $5P_{3/2}$ state and the $nS_{1/2}$ state. The splitting between the two peaks gives the generalized Rabi frequency of the detuned 780-nm MOT trapping beams. The width of the taller, two-photon resonance peak is limited by the laser linewidth, but it power broadened in this case to about 6 MHz. Further discussion of the nature

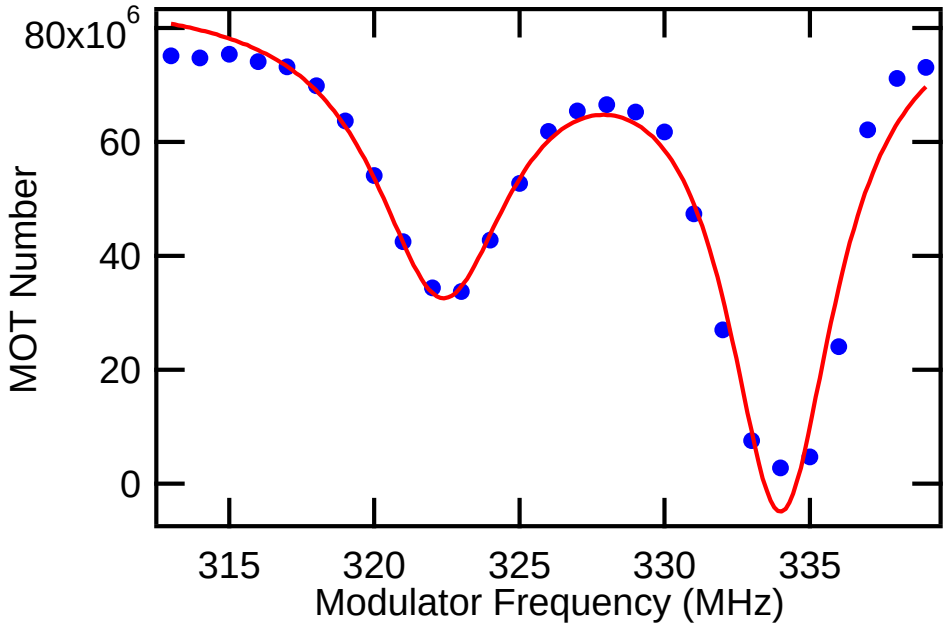

Figure 5.1: MOT number versus blue light frequency, as given by the frequency applied to the electro-optic modulator that we use to shift our 960-nm light frequency prior to doubling. The drop in MOT number shows the Autler-Townes spectrum of the excitation to the $50S_{1/2}$ state. The solid curve shows a fit to a sum of two Lorentzian functions.

of the Autler-Townes spectra similar to those that I measure is presented in [2]. Because Rydberg excitation is related to increased loss from the MOT, I observe the spectrum as a decrease in atom number. I subtract this spectrum from the baseline MOT number in order to yield a more traditional spectrum of peaks rather than dips.

I can then investigate the excitation rate to the Rydberg level by holding the blue laser on the frequency of the two-photon resonance and scanning the time of the excitation pulse. I observe that the MOT number decreases as I increase the

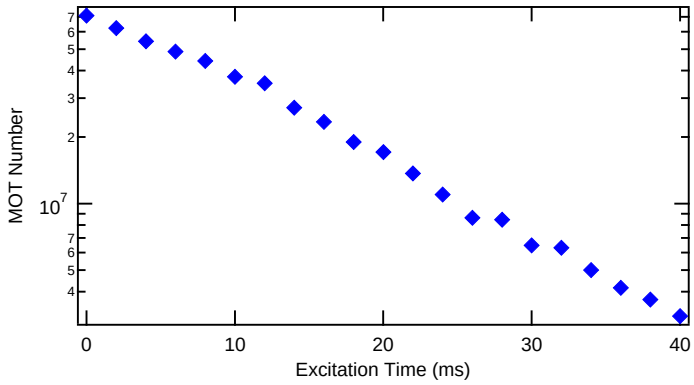

Figure 5.2: The MOT number versus excitation time. The log scale on the y-axis shows that the number decays as a simple exponential.

blue light pulse time. Figure 5.2 shows a scan of the MOT number versus the length of the Rydberg excitation pulse. The curve shows an exponential decay over time, with a decay time on the order of tens of milliseconds. By fitting these curves for different electric field magnitudes, ranging from about 0-2 V/cm, and thus different dipole moments, I am able to determine the variation in excitation rate as I increase the induced dipole moment.

5.3 Excitation Rate Data

I determine the rate of Rydberg excitation by taking the natural log of the ratio of the number left in the MOT after 2 μs to the number remaining after 20 ms, and then normalizing this to the rate observed at zero field. This gives a normalized decay rate of the MOT. This also has the benefit of providing a decay rate number with only 2 experimental cycles, rather than the 25 cycles needed to generate the plot in Fig. 5.2. Because the blackbody ionization time, which leads to atom loss, is

much longer than both the excitation time of the atom to the Rydberg level and the 140-μs lifetime of the $50S_{1/2}$ Rydberg state, I consider the observed MOT decay rate as the blackbody photoionization rate, scaled by the saturation number of Rydberg atoms in the system. I calculate the excitation rate by approximating the excitation cross-section as presented in Chapter 4, which yields an excitation time from the $5P_{3/2}$ state to the $50S_{1/2}$ state of 4 μs for these experiments, based on laser power and detuning parameters. As I increase the external electric field, I induce a larger and larger dipole moment, leading to DDIs, which suppress the saturation Rydberg number, and therefore the observed MOT decay.

I calibrate the electric field by fitting the shift of the two-photon resonance frequency to the calculated Stark map, and use that to calculate the induced dipole moment of the atoms at a given electric field. Fig. 5.3 shows this fit, as well as the calculated dipole moment. It is apparent from the fit that the fields I have used are in the small-field regime, in which the Stark shift is quadratic in electric field strength, and the dipole moment depends linearly upon the field strength. I apply a maximum electric field of ~ 1.5 V/cm. I have also obtained an estimate of field strength by modeling the electrode configuration in Simion, as discussed in Appendix B, which is consistent with the calibration obtained from fitting the experimental Stark shift.

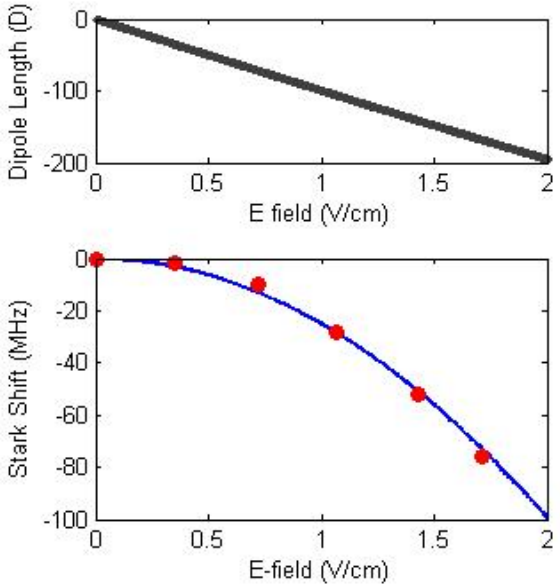

Figure 5.3: The Stark energy shift and induced dipole moment for the $50S_{1/2}$ state of Rb. The top graph shows the calculated dipole moment, while the bottom graph shows the experimentally observed Stark shift (red markers) fit to the calculated Stark shift curve (blue solid line).

5.4 Analysis

I used two methods to analyze this data. First I performed a simple analytical fit by calculating the number of Rydberg blockade bubbles, or superatoms [14], would fit in a given volume, and how that number changed over time. I fit the data to this bubble number.

I also analyzed this data by performing a Monte-Carlo simulation of the Rydberg excitation. By initializing the system with parameters similar to our experimental parameters, I can simulate the excitation and decay of the system as DDIs increase.

5.4.1 Blockade Bubble Method

When I excite a Rydberg atom, its interactions cause it to suppress the excitation of nearby atoms, as described in Chapter 1. This blockade causes the atom to form an effective superatom [14] or a "bubble" of blockaded area, where only one atom may be excited. The volume of this blockade bubble describes the potential maximum number of Rydberg excitations in a given volume, and can be approximated by dividing the given volume by the volume of the bubble.

I calculate the Rydberg blockade radius by solving for r_{block} in the equation

$$\Gamma = \frac{c_3}{r_{block}^3} + \frac{c_6}{r_{block}^6}, \tag{5.2}$$

where Γ is the dominant linewidth, in our case the laser linewidth, and c_3 depends upon the dipole moment squared. This calculation yields a blockade bubble volume given by

$$\frac{4}{3}\pi r_{block}^3 = \frac{\pi}{3}\frac{c_3}{\Gamma} \pm \sqrt{\frac{c_3^2}{\Gamma^2} + \frac{4c_6}{\Gamma}}, \tag{5.3}$$

which varies $\sim d^2$ due to the linear dependence on c_3. Because c_6 does not depend upon the dipole moment and does not change with applied field, it acts as an offset on both the blockade radius and the bubble volume. I calculate the number of blockade superatoms in a given volume and subtract that number from the total number of atoms in that same volume to determine how the percentage of Rydberg atoms would change as the blockade radius increases. This yields a smoothly decreasing function, which shows a saturation as the system approaches maximal blockade. I use the

DDI magntiude as an adjustable parameter in the fit, which gives a qualitative fit, though not a quantitatively rigorous one.

5.4.2 Monte-Carlo Simulation of Rydberg Atoms with DDIs

I consider a system of N atoms, where N is chosen to be large while keeping calculation time low (typically 1000), randomly placed in a cubic box with volume $r_0^3 N$, where r_0 is the average separation between two particles, yielding an average density of r_0^{-3}. I consider an r_0 of 3 μm, which is similar to the average density of the MOT. I then loop through the atoms to simulate the time dynamics of the excitation. For each time step, I define a random number that is compared to the probability of exciting the atom, given by τ_{ex}/t_{step}, where τ_{ex} is the excitation time of the Rydberg state and t_{step} is the length of the time step. For each time step, I cycle through all the atoms and determine whether or not each is excited by comparing the probability of excitation with the random number. When an atom is excited, it is added to a new vector of excited state atoms.

I simulate the spontaneous decay of the atoms by defining another random number and comparing it to the probability that the atom will decay, given by τ_{life}/t_{step}, where τ_{life} is the lifetime of the state. For the $50S_{1/2}$ state, the lifetime is about 140 μs, calculated from [21].

I then include the blockade effect by adding an additional excitation condition. I compute the interaction energy between a test atom and all the other excited atoms in the system and if the interaction is above a certain energy threshold, the atom

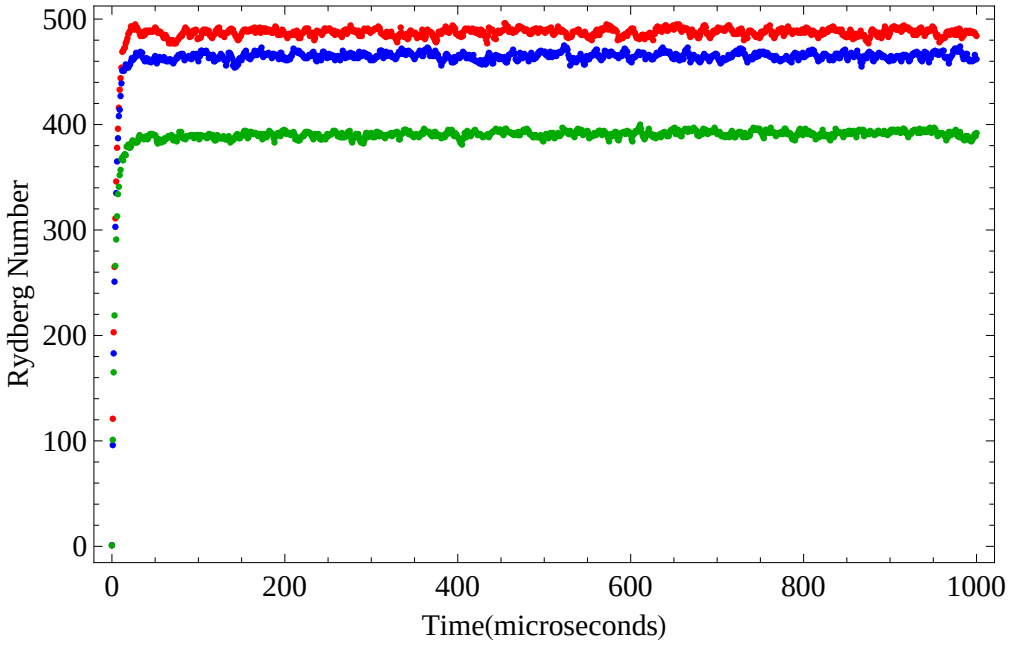

Figure 5.4: The excited Rydberg number versus time for three Monte Carlo simulations, showing how the saturation number changes with applied field. The red curve shows the excitation with no applied field, the blue curve shows excitation in a 0.9 V/cm field, and the green curve shows excitation in a 1.8 V/cm field.

is not excited. I run this simulation for various values of N to ensure that there are no artifacts of finite system size on the simulation.

For each dipole moment, I compute the number of atoms excited at a given time and run the simulation for 1000 1-μs steps. I find that the excitation saturates after <10 μs and that the saturation Rydberg number decreases as the dipole moment increases, as expected. Figure 5.4 shows the results of several simulations for different electric field values, considering only the DDI. Because the van der Waals interaction should not change as the electric field changes, I disregard it for now. I will discuss the van der Waals interaction and how it appears in this system in

more detail in the next chapter. As the electric field increases from 0 to 2 V/cm, the saturation number decreases. I then consider that the experimentally measured excitation rate is the blackbody ionization rate scaled by the saturation Rydberg number and plot the experimental data versus the simulation results for different dipole moments.

True Rydberg blockade is not a step-wise effect like this, but rather a gradual increase of the excitation probability as the atoms move further apart. Theoretically, the threshold for blockade should be set by the natural linewidth of the Rydberg transition, which is $\sim$ 10 kHz. In this system, however, the dominant linewidth should be that of the lasers. The linewidth of the 960-nm laser is about 500 kHz and the linewidth of the 780-nm laser is $<$2 MHz, as measured by self-homodyne detection, which is described in Appendix A, and was limited by the length of the fiber I used in the measurement. The 780-nm laser has a specified typical linewidth of 1 MHz. These linewidths suggest that the blockade cutoff should be $\approx$ 1 MHz.

I considered how motion might affect the time dynamics of the states of the atoms in my simulation. The velocity distribution of the atoms is calculated from a Maxwell-Boltzmann distribution at the temperature of the MOT, which is about 200 μK, which corresponds to a velocity of 0.17 μm/μs. Given this velocity, the atoms would move a total of $\sim$ 24 μm every lifetime of the state. Additionally, this velocity is slow enough that the atoms will move only 6% of the average interparticle spacing each time step of the simulation. If this motion has an effect, it would primarily be to re-randomize the atoms each lifetime, so it is unlikely that motion plays a role in the qualitative results of this simulation.

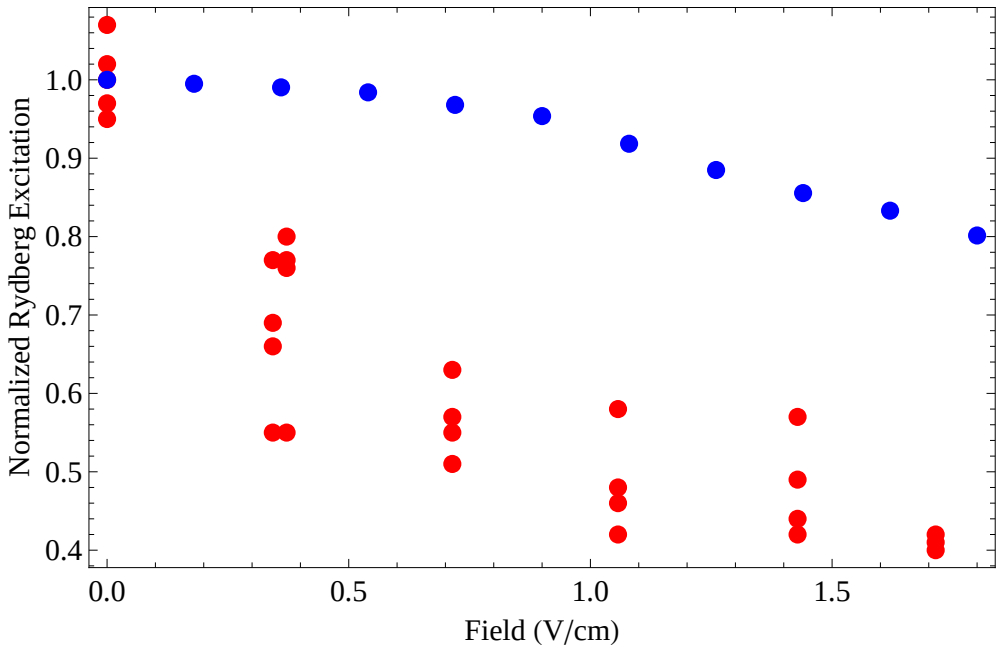

Figure 5.5: Experimental data (red) with data from the Monte Carlo simulation for the $50S_{1/2}$ Rydberg state (blue).

Figure 5.5 shows the results of a Monte Carlo simulation for the $50S_{1/2}$, using a blockade cutoff of 1 MHz, considering the strength of the DDI from my Stark map calculations. I fit the experimental Stark shift to the calculation to determine what dipole moment I induce for each applied voltage. These simulation data show much less suppression of the excitation than do the experimental data. This difference suggests that I see a DDI experimentally that is larger than that predicted solely by DDIs between 50S Rydbergs.

5.4.3 Transitions to Nearby P States

One potential mechanism that could enhance the experimentally-observed DDI is a transition from the 50S state to a nearby P state. Background black body ra-

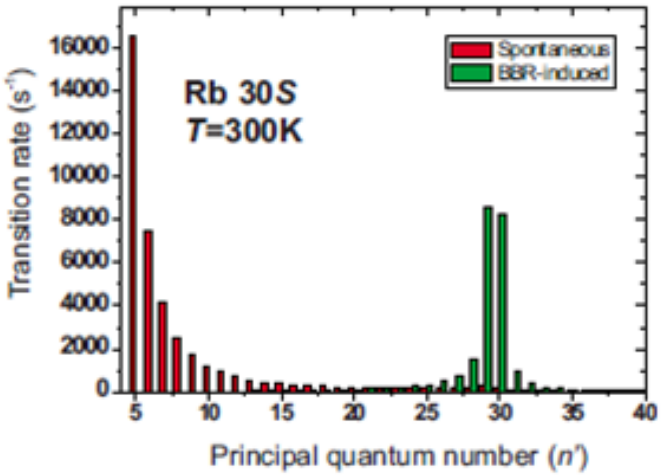

Figure 5.6: Graph of how black body radiation effects the possible transitions from the Rydberg 30S state, from [8].

diation, in addition to causing photoionization, can also cause transitions to nearby Rydberg states. Because I start in an S state, the primary loss would be to the Rydberg P states. Because these states are still Rydberg states, and not ionized, their dipole moments will affect suppression of the excitation, because the dipole moment of the P state is larger than that of the S state.

Figure 5.6 shows numerically-calculated rates of spontaneous emission from the rubidium $30S$ state to nearby P states [8]. Without considering black body transitions, the atoms decay primarily to the lowest n states. With black body transitions, the states decay primarily to the two nearest n states. This effect suggests that background black body radiation can cause a strong probability to transition to a Rydberg P state, which has a dipole moment up to 5 times larger than that of the S state, rather than back to the ground state.

I calculated the black body transition time for the $n = 50$ Rydberg state using

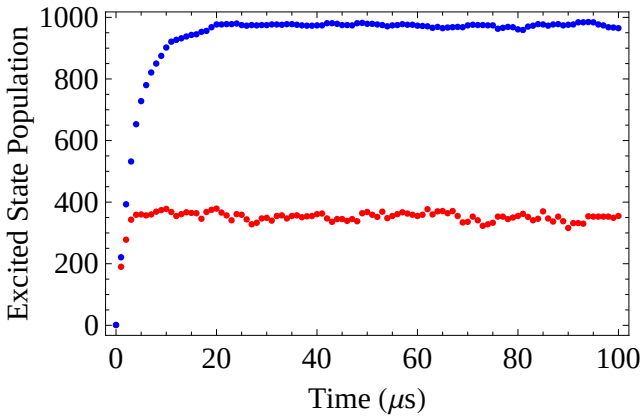

Figure 5.7: Simulations of the Rydberg excitation with and without the losses via black body transitions to the P state. The red curve shows that we lose about 65% of our S-state population to the P state.

the technique used in [21]. The result of this calculation is an expression for the black body transition time that is independent of angular momentum:

$$\frac{1}{\tau_{nl}^{bb}} = \frac{4\alpha^3 k_B T}{3n^2}, \tag{5.4}$$

where α is the fine structure constant, k_B is the Boltzmann constant, $T = 300$K, and n is the principal quantum number. This expression yields a black body transition time to all possible states of about 500 μs for the $n = 50$ Rydberg state. I simulated the dynamics of the excitation using my Monte Carlo simulation, in the absence of DDIs, adding $1/\tau_{nl}^{bb}$ as an additional loss rate. Figure 5.7 shows the result of this simulation with and without the black body transition. I see that when I include the transition to the P state, the excitation saturates at a lower number. Without P-state transitions, the system saturates in a time on the order of $1/\Gamma$. This slope is preserved when I add the P-state transition, as the excitation time from the 5P

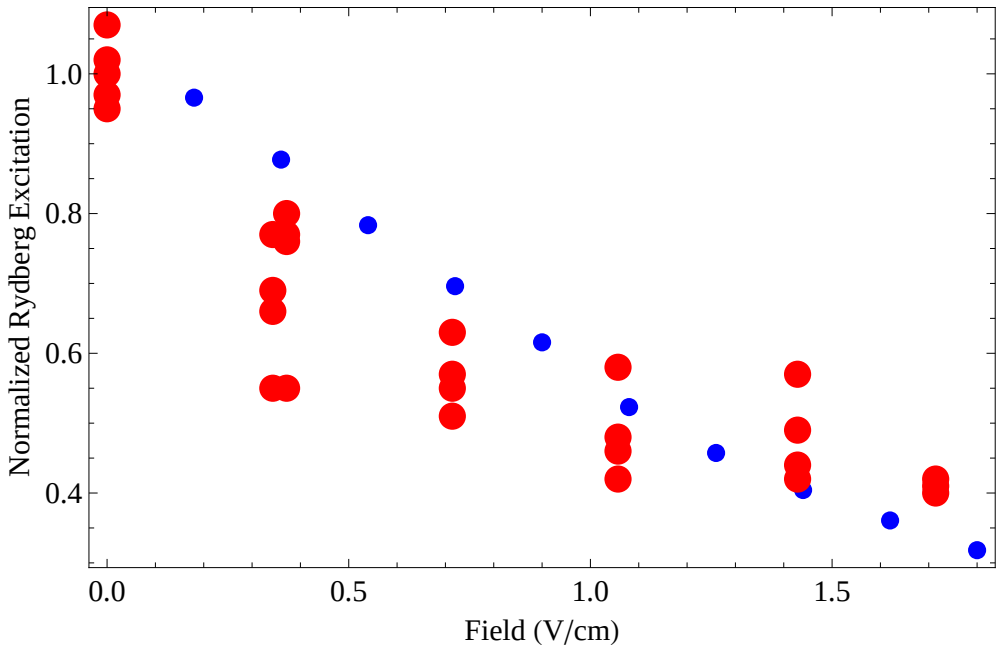

Figure 5.8: Experimental data (red) with data from the Monte Carlo simulation considering a 65% population of the P-state.

state to the 50S state is still the shortest time scale, but the lower saturation number means that the system reaches this steady state faster. I found that I lost about 65% of the atoms to the P state transition, suggesting that up to 65% of our DDI could be from the stronger P state interaction, rather than the S state interaction. Figure 5.6 shows that the primary loss from the nS state is to the nP or $(n-1)$P state, so I considered transitions only to the 50P state, as the formula $d \sim n^2 e a_0$ suggests that there will be only a 4% difference in dipole moment between the $n = 49$ and $n = 50$ states.

I then re-ran my original Monte Carlo simulation considering atoms interacting with a mixture of 35% S state and 65% P state. Figure 5.8 shows the result of this simulation. While the Monte Carlo simulation does not represent an analytical fit,

the simulation fits much more closely when I consider the P state enhancement of the DDI.

These simulations show that, qualitatively, the decrease in excitation rate as we increase electric field can be explained by increasing the induced dipole moment. I do not consider the van der Waals interaction because it should be approximately constant in electric field. I can, however, further explore the importance of the van der Waals interaction by exploring excitation to different ns. Because the van der Waals interaction depends upon n^{11} and the DDI depends upon n^4, investigating different ns will give insight into the difference between the effects of the van der Waals interaction and the DDI.

Chapter 6

Experimental Data from Multiple n Levels

6.1 Overview

The data I present in the previous chapter do not take into account the field-independent interactions between Rydberg atoms. Using the parameters at which I perform the experiment, the van der Waals interaction strength ranges from being the sole interaction in the system, when the field is zero, to being on the same order of strength as the DDI, when the field is tuned to a higher, yet still small, value.

6.2 Data for $n = 41$ and $n = 56$

It is necessary to open the master laser to manually rotate the grating in order to change the wavenumber to access different n levels, as discussed in Chapter 4. I collected further excitation rate data at the Rydberg levels 41S and 56S. Data collection and processing was similar to that described in previous chapters. Because the experiment had been offline for a number of months between this collection and the previous data collection, I re-calibrated the electric field offset and magnitude by fitting the frequency shift to the calculated Stark map. Because I had approximately a factor of two less power in the blue laser for these excitation data, I considered the ratio between the MOT number after 2 μs and 40 ms of excitation in order to extract

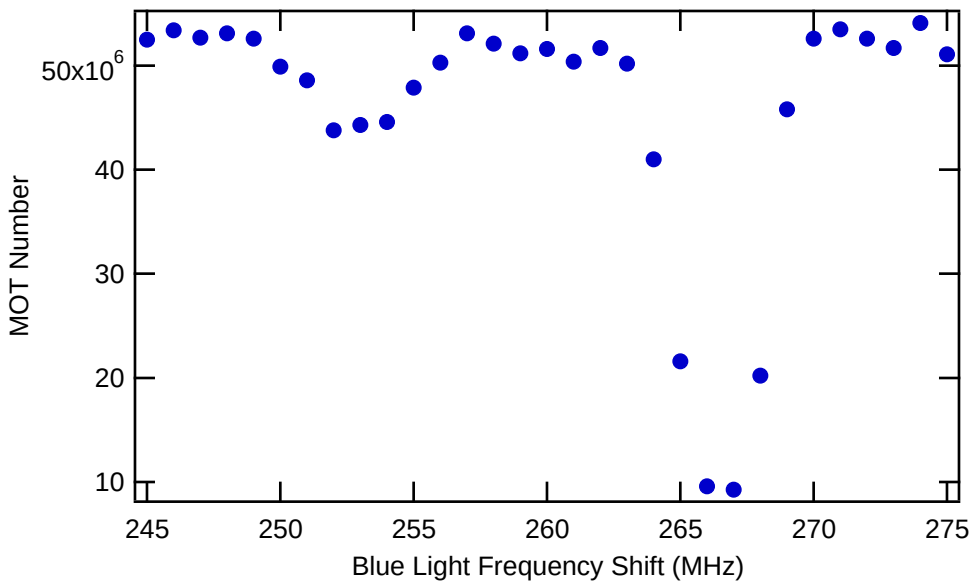

Figure 6.1: Autler Townes spectrum of the $41S_{1/2}$ state, for a blue-light excitation time of 50 ms.

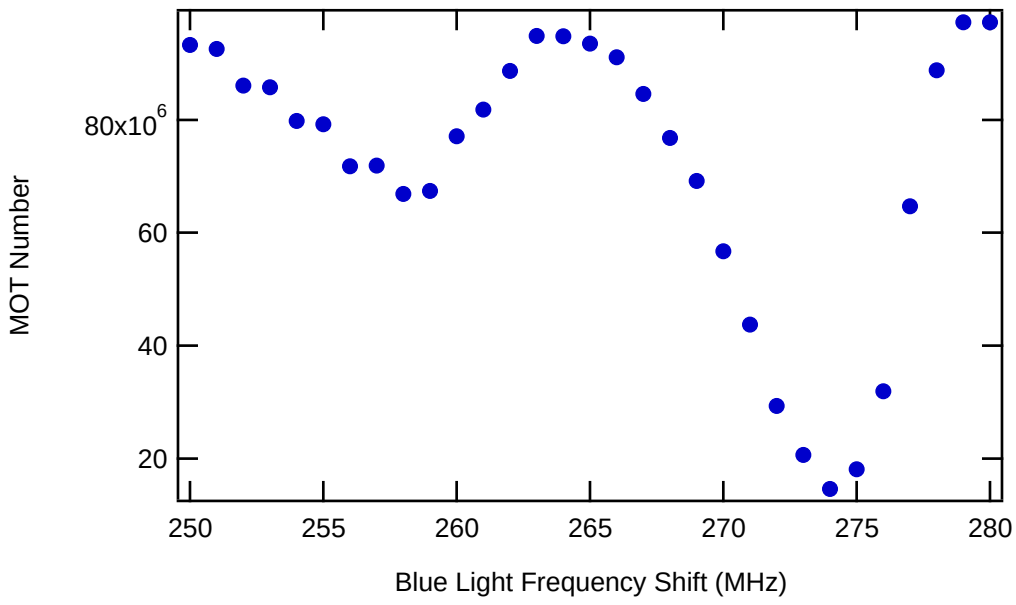

Figure 6.2: Autler Townes spectrum of the $56S_{1/2}$ state, for a blue-light excitation time of 50 ms.

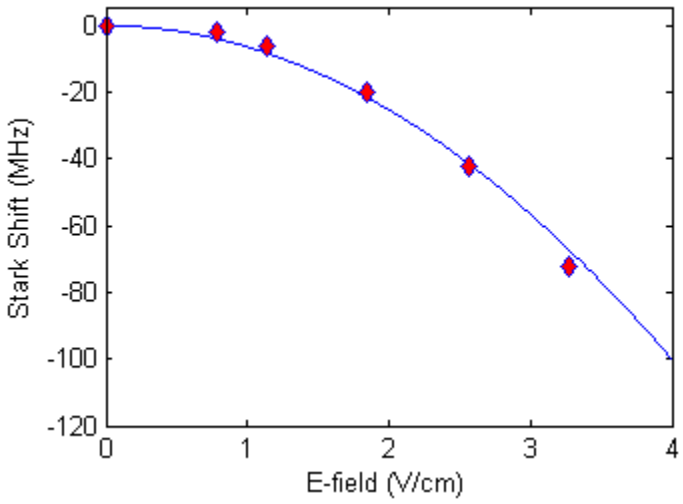

Figure 6.3: Experimental Stark shift of the $41S_{1/2}$ state, fit to calculated value. From this, I was able to calibrate the relation between voltage and electric field, and also determine the induced dipole moment.

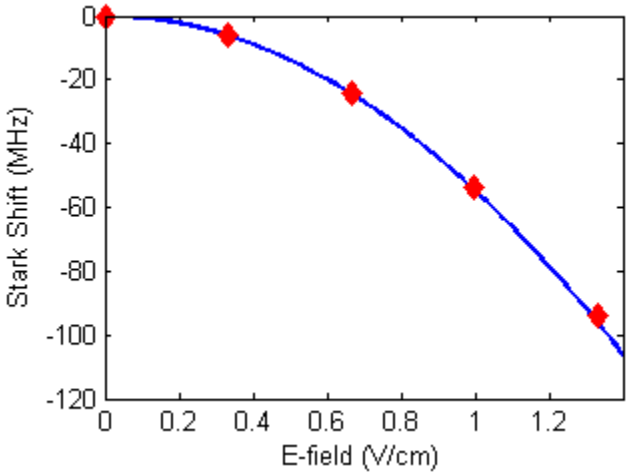

Figure 6.4: Experimental Stark shift of the $56S_{1/2}$ state, fit to calculated value.

the excitation rate. Figures 6.1 and 6.2 show the Autler-Townes spectra of the 41S and 56S states, respectively, while 6.3 and 6.4 show the experimentally-measured Stark shift of the two levels. These data were taken in the same manner as those presented in Chapter 5.

I also used ~ 4 mW of blue light, as the coupling to the doubler cavity had changed since replacing the TA chip in the Sacher Lasertechnik system. The slight decrease in blue laser power did not seem to affect my ability to excite the atoms to Rydberg levels noticeably. I used a two-photon transition, as before, with slightly altered MOT parameters, in order to maintain a MOT with a number of about $5 - 8 \times 10^7$ with a diameter of about 2 mm. The cloud had a density of about $6{\times}10^{11}$ cm^{-3}, which corresponds to an average interparticle spacing of 2.5 μm.

Figure 6.5 shows the experimental data plotted with a bubble method curve. The data show a steeper drop in the excitation rate for the $n = 56$ level than for the $n = 41$ level, which is consistent with the increase in DDI as n increases. The experimental data also shows the same qualitative curve that I saw in the $n = 50$ data in the previous chapter.

I was also able to tune the laser to excite the 61S Rydberg state, but the data are noisy and this level has an avoided crossing at a field magnitude of about 0.9 V/cm, so I decided not to pursue further analysis of this data beyond the comparison of the zero-field excitations.

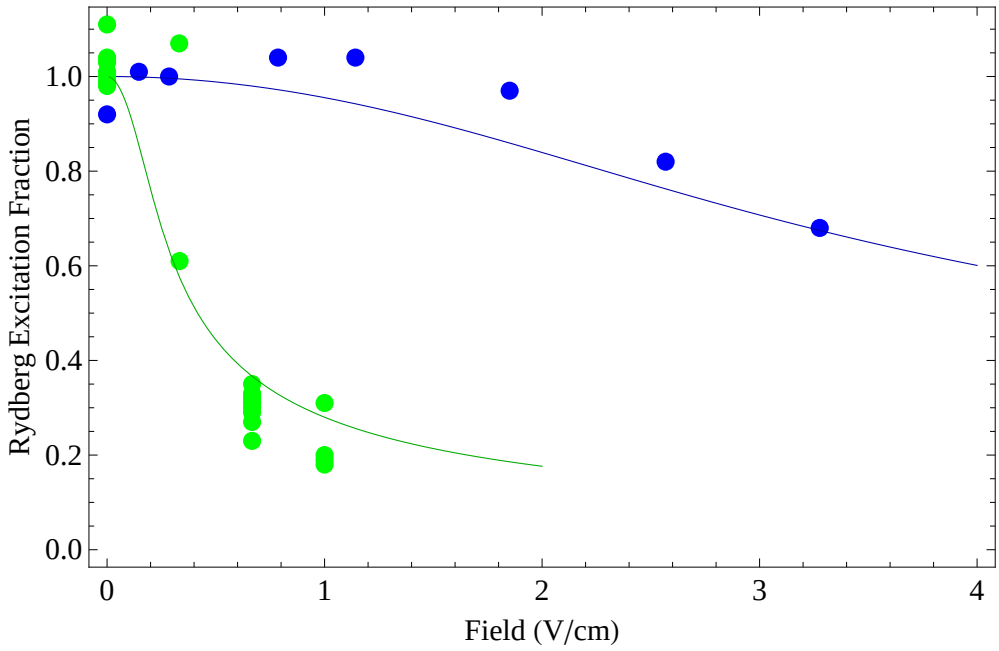

Figure 6.5: Normalized Rydberg excitation rate as a function of applied electric field for the 41S (blue dots) and 56S (green dots), plotted with curves (solid lines, blue for 41S and green for 56S) calculated by the blockade bubble method described in Chapter 5.

6.3 Van der Waals Interaction As a Function of n

In the previous chapter, I simulated the dynamics of the system with a Monte Carlo method considering only the DDI between Rydberg atoms in a variable DC electric field. This simulation does not take into account the zero-field Van der Waals interaction, which can be large for Rydberg atoms. The blockade bubble method of estimating Rydberg blockade suggests that the Van der Waals interaction should just be an offset on the blockade effect, independent of applied field.

6.3.1 Theoretical Treatment of the Van der Waals Interaction between Rydberg Atoms

In Chapter 1, I discussed the phenomenon of Förster resonances in Rydberg gases. In [60], the authors present an expression for the interaction energy between two Rydberg atoms, as a function of interparticle separation, R, and energy defect or detuning of the energies in the system from the Förster resonance, Δ:

$$U_{\pm}(R) = \frac{\Delta}{2} \pm \sqrt{\frac{4U_3(R)^2}{3} + \frac{\Delta^2}{4}}. \tag{6.1}$$

Here, $U_3(R)$ is the DDI term, which dominates when Δ is small, or when R is small. For non-zero Δ, this energy defect causes the interaction energy to drop at long-range. In this situation, $U_+(R)$ converges to $-4U_3(R)^2/3\Delta$, which scales as $1/R^6$ and is the usual van der Waals interaction term. In this case, $c_6 = -4c_3^2/3\Delta$ [60].

Outside of this intuitive understanding of the van der Waals interaction, it is possible to calculate the exact interaction between Rydberg atoms in the absence

of an electric field, as a function of n and atomic properties. In [54], the authors calculate the exact interaction between Rydberg atoms of various angular momenta and symmetries. They expand the interaction potential and find the non-vanishing terms for each case. For Rydberg S states, the longest-range term is the c_6/r^6 term, and for rubidium Rydbergs between $n = 15$ and $n = 235$, describes a repulsive potential. The authors also found a dependence of the overall coefficients on a power of n, which describes how these interactions should scale as n changes.

6.3.2 Experimental Observations at Zero Field

Using calculations in [54], I determine that the van der Waals interactions vary proportionally to n^{11}, so I would expect the 61S level to have a van der Waals interaction ~ 100 times greater than that of the 41S level.

Figure 6.6 shows the zero-field excitations for the four investigated levels. The slight variation could be attributed to differences in excitation matrix element, which scales with n^{-3}, but does not show the strongly n-dependent behavior that I expect from naïve calculations. This result suggests that there is more theoretical work needed to determine how this detection technique probes the van der Waals interactions of the system.

In Chapter 5, I discussed the likelihood that some of the Rydberg atoms make black-body-stimulated transitions to nearby P states. Because the van der Waals interactions between P state atoms have signs that vary with symmetry, it is possible that the P state transitions wash out the van der Waals effect in the system. Using

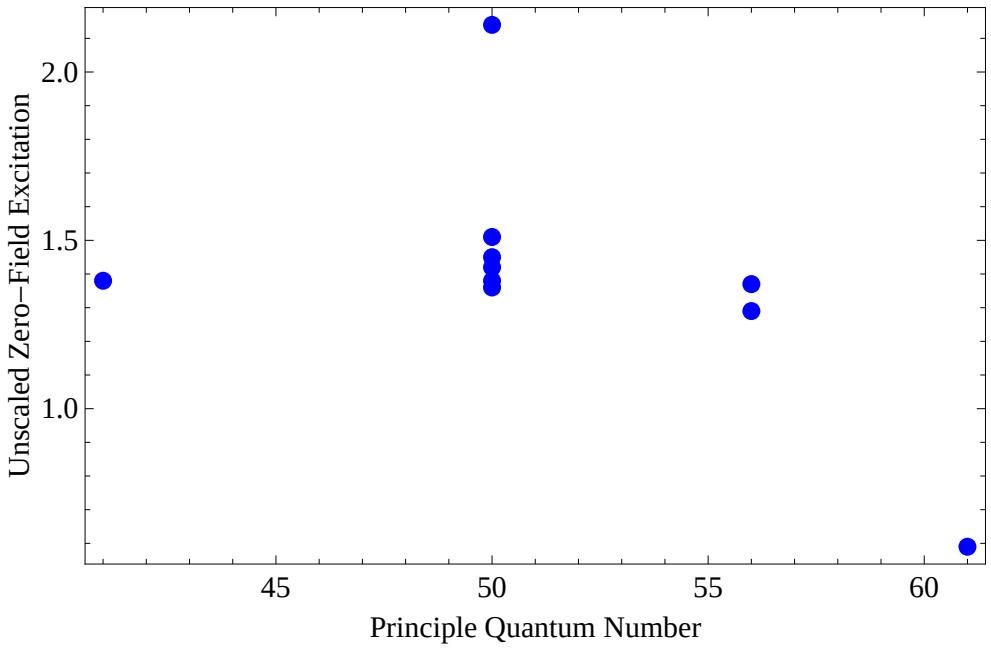

Figure 6.6: Plot of the experimental zero-field excitation rate before normalization. Each point represents a single excitation rate data point. This gives an idea of how van der Waals interactions affect our system.

the values given in [54], I can calculate how the van der Waals coefficients would change if I consider the contribution of P-state Rydbergs. Because of symmetry considerations, I only need to consider two of the possible twelve symmetry states for the P state. I also only need to consider the c_6 coefficients, as both of these symmetry states have vanishing c_5 coefficients. I calculate the c_6 coefficient for both the fully S-state case, and the case where 65% of the interaction is due to the P state and 35% of the interaction is due to the S state.

Before I can calculate the coefficients, I first must determine which symmetry states are allowed. Because the atoms start in the nS state, their interaction symmetry is either ${}^1\Sigma_g^+$ or ${}^3\Sigma_u^+$ [54]. This symmetry suggests selection rules that govern which symmetries will be allowed when the atoms transition to the P state. The table in [54] shows the available symmetry states for the P state. By selection rules for molecular transitions [30], Σ^+ can only go to Σ^+ and g can only go to u. Additionally, only $1 \to 1$ and $3 \to 3$ are allowed. Thus, none of the P-states with Σ symmetry are allowed. Additionally, only $\Sigma \to \Sigma$ and $\Sigma \to \Pi$ are allowed, which eliminates the Δ states. From the other selection rules, I can determine that only ${}^1\Pi_u$ and ${}^3\Pi_g$ are allowed, which both have the same coefficients. For these states, the c_5 coefficient vanishes and the c_6 coefficient is almost an order of magnitude smaller than that of the S states.

I found that for $n = 40$, the interaction with P-state transitions is 48.7% of that with only S-state interactions included. For $n = 50$ and $n = 60$, the interactions are 47.5% and 46.7% of the S-state interaction, respectively. This calculation shows that mixing P-state interactions into the system will drastically decrease the van

der Waals interactions. The mild n-dependence of this effect suggests that black body transitions to P states could help explain the apparent lack of effect from the van der Waals interaction in this system.

6.4 Black-Body Transitions to Nearby Rydberg States As a Function of n

The previous chapter discusses how room-temperature black-body radiation can cause transitions to nearby P-states in this system. Because the black-body transition time is $\sim n^2$, I had to simulate the effects of black-body transitions to determine if the different n levels should be simulated with differing amounts of added P-state DDI. The lifetime, however, also varies with n, scaling with $n^{2.94}$[21], so over the range which I investigated, the black-body transition time varies similarly to the Rydberg state lifetime.

Figure 6.7 shows the variation of the S-state fraction as a function of n. For each n, I simulate the Rydberg S-state population as a function of time using Monte Carlo analysis, fit the data, extracted the saturation number, and divided the saturation Rydberg S-state number with P-state transitons by that without this additional loss. I repeat this simulation ten times for each n, resulting in the spread of points seen in the figure. The figure clearly shows that there is little variation of S-state fraction over the range of n levels I probed.

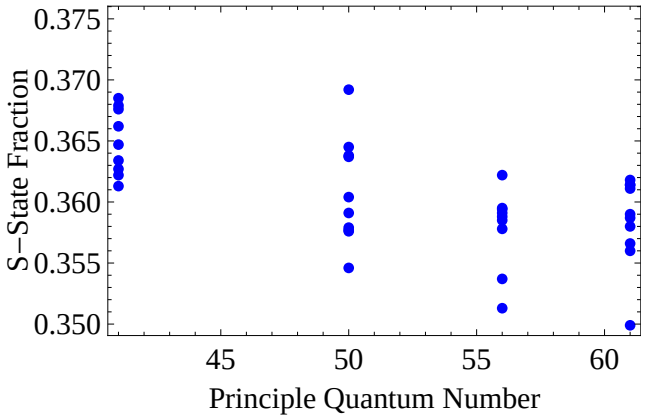

Figure 6.7: Results of simulations of the black-body transition losses from the S state for various principle quantum numbers. Each n was simulated 10 times, and all the resulting data points are plotted.

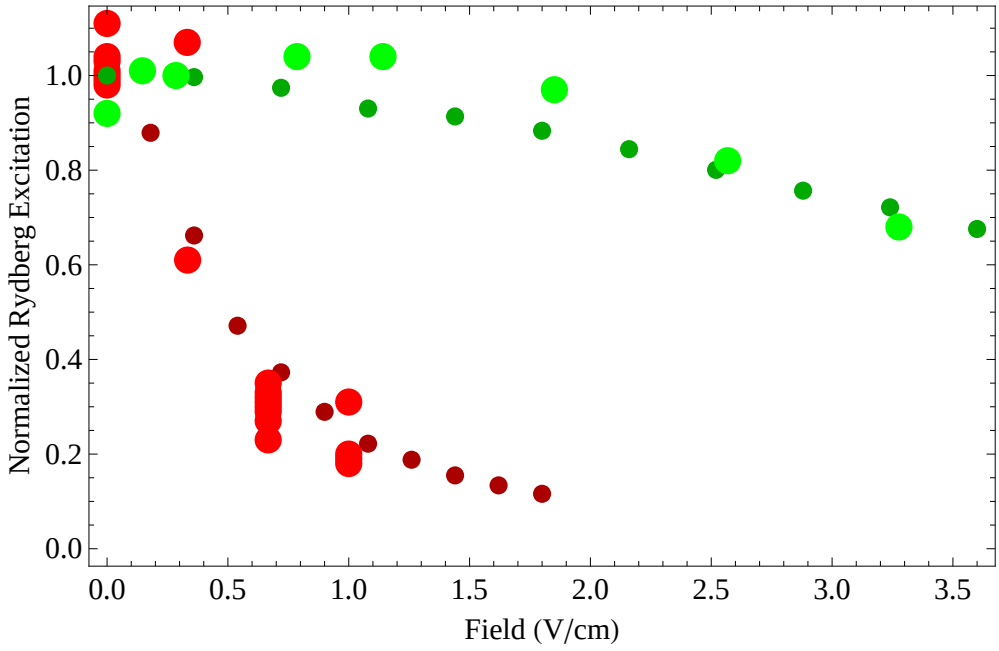

Figure 6.8: Experimental data (large, lighter points) plotted with Monte Carlo simulations (small, darker points) for $41S_{1/2}$ (blue) and $56S_{1/2}$ (green), versus applied electric field.

6.5 Analysis By Monte Carlo Simulation

Figure 6.8 shows the 41S and 56S S-state data, plotted with data simulated by Monte Carlo analysis. I consider 500 atoms in the simulation, excited for 500 μs, interacting via DDIs, with 65% P-state DDI and a blockade cutoff of 1 MHz. Because the MOT parameters for the experimental data for these levels were different, the average interparticle spacing is ~ 2.5 μm. The simulation shows that I can attribute the suppression of excitation to the increased DDI as I increase the electric field magnitude. The 41S state shows less suppression of the excitation as it has a lower DDI, while the 56S state shows a higher suppression, due to higher DDI.

This data and analysis corroborates what I saw in the previous chapter: the decrease in the excitation to the $50S_{1/2}$ state is due to increased DDI with enhancement from black-body transitions to a nearby P-state.

6.6 Conclusions

The work done in this thesis shows a step towards designing variable-DDI states which can be used to simulate novel quantum phases of matter in bosonic systems. I investigated two ways of creating a variable-DDI state using Rydberg atoms, first by inducing a dipole moment with an external DC electric field, and then by calculating the effects of dressing the ground-state atoms with a beam that excites a small fraction to the Rydberg state. Both showed tunable control over the DDI. I also reported early work in implementing a field-tuned DDI in cold Rydberg atoms in states with multiple ns.

The Stark map work shows explicitly how the addition of an external DC electric field breaks the spherical symmetry of the Rydberg atom and induces a dipole moment that is approximately proportional to the applied field strength for sufficiently small fields. These calculations agree with previous theoretical studies of alkali Rydberg atoms and gave me an important tool to calibrate and characterize my experimental data. Using the Stark shift plot to fit the experimentally-observed Stark shift, I am able to predict what DDI I should expect for a given Rydberg state in a given electric field. Because I use high-n Rydberg states, I can use small fields, <5 V/cm, to induce large changes in the DDI, which avoids issues of dielectric breakdown.

The investigation of Rydberg-dressed atoms shows promise in creating atomic states that have DDIs that are sufficiently large to see the effects proposed in the theory papers I discussed in Chapter 1. The unusual R-dependence of the interaction curves also suggest new solid state physics that I or other researchers could realize. Recently, a group in Pisa, Italy attempted to realize a dressed-Rydberg state in the lab, but found their experimental parameters insufficient, and are currently trying to improve before trying again [3]. The group of Tilman Pfau in Stuttgart has seen evidence of anisotropic expansion in a gas of Rydberg-dressed atoms, as well [43]. In Chapter 3, the parameters we used in calculating interesting interactions would require laser powers higher than our lab can produce, due to the strong preference for high Rabi frequencies and the drawbacks of using a two-photon Rabi frequency.

The second part of the thesis describes the experimental data I have collected implementing the Stark-shifted Rydberg states to show variable DDIs in Rydberg

S states. Data taken at $n = 50$ shows a significant suppression of the Rydberg excitation as I increase the electric field magnitude, which qualitatively agrees with a simple analytical model of the DDI effects on the number of potentially excited Rydbergs. I also saw an effect of black-body transitions to nearby P states, which enhances the observed DDI. Considering this black-body enhancement, the experimental data agrees well with a Monte Carlo simulation of my system, interacting via variable DDIs. Because we do not measure Rydberg states directly, we cannot determine exactly which Rydberg states are causing the effects we see. This, along with the apparent large contribution of P-state Rydbergs, makes extracting highly quantitative results challenging.

Data taken at 41S and 56S also show excitation suppression that agrees with what I expect from a variable-DDI system. I see a change in the amount of suppression for a given electric field magnitude as we change n, which agrees with theoretical predictions of the n-dependence of the dipole moment of Rydberg atoms. I also looked at the n-dependence of the black-body transitions to show that, over the range of n that I consider, the variation in P-state fraction is negligible. I also looked at the zero-field excitation to show that I do not see the strongly n-dependent effect that I predict from initial calculations of the van der Waals interaction in rubidium Rydbergs, but that black-body transitions to P states could offer an explanation for this. The data taken at different n's also shows a good agreement with Monte Carlo simulations of our system interacting with variable DDIs.

This thesis represents preliminary work towards realizing a variable-DDI system which could be used to study novel quantum phases of matter. The experimental

data shows that external electric fields are a promising potential avenue by which future researchers could change the long-range interactions between trapped atoms and see the phase transitions proposed in Chapter 1.

Appendix A

Blue Light Stabilization

In order to stabilize the laser frequency enough that we could consistently excite the narrow Rydberg resonance, we had to use a Pound-Drever-Hall cavity transfer lock. Briefly, the locking scheme is as follows: A Fabry-Perot cavity is stabilized by feeding back the error signal from a stable 780-nm laser. A 960-nm laser is then stabilized by feeding back its error signal from the stable cavity. The doubler cavity is then pumped with this stable, 960-nm light, which also serves to stabilize the length doubler and the resultant 480-nm light. We have also determined that our laser system linewidth is <1 MHz by self-homodyne detection.

A.1 Generation of 960-nm light

We generate 960-nm light from a home-built diode laser, which is amplified with a tapered amplifier chip. A commercial single-mode laser diode is placed in an external cavity in a Littrow configuration and injected into a Sacher TEC-300 run as a tapered amplifier, as described in Chapter 4. Most of the light goes through a system of mode-matching optics and pumps the doubler cavity so that we can use the resulting blue light, but a small portion of amplified 960-nm light is picked off and sent to locking electronics to stabilize it.

The Sacher laser is modified as follows to perform as a tapered amplifier, rather

than an injection-locked system: The grating is removed and replaced with a gold mirror inside the laser body. This mirror is fixed down with no degrees of freedom, and optimization of the injection is performed by overlapping the backwards-propagating beam from the diode with the injected beam from the master laser. Images of this laser system were shown in Chapter 4. We decided on this configuration after experiencing noise and large linewidths in the Sacher laser. This problem was not resolved by injection locking the high-power laser to a lower-power homebuilt laser. In the tapered amplifier configuration, we do not need to match frequencies, and we see neither the noise on our cavity signals nor the large linewidth measured previously. A discussion of the linewidth measurement by self-homodyne detection is below.

A.2 Stabilization of the Fabry-Perot cavity

The Fabry-Perot cavity is a 0.5-m Invar cavity in a confocal configuration. The mirrors on either end are spherical mirrors with a radius of curvature of 0.5 m and a broadband dielectric coating designed to reflect both 780-nm and 960-nm light with sufficient reflectivity to generate a narrow signal for locking. The long length of the cavity provides ease in generating a signal for both 780-nm light and 960-nm light within the 150-MHz free spectral range. However, there is a drift in the cavity length over time. In order to combat this, we stabilize the cavity length by feeding back to a piezoelectric transducer that makes small changes to the length of the cavity at one mirror.

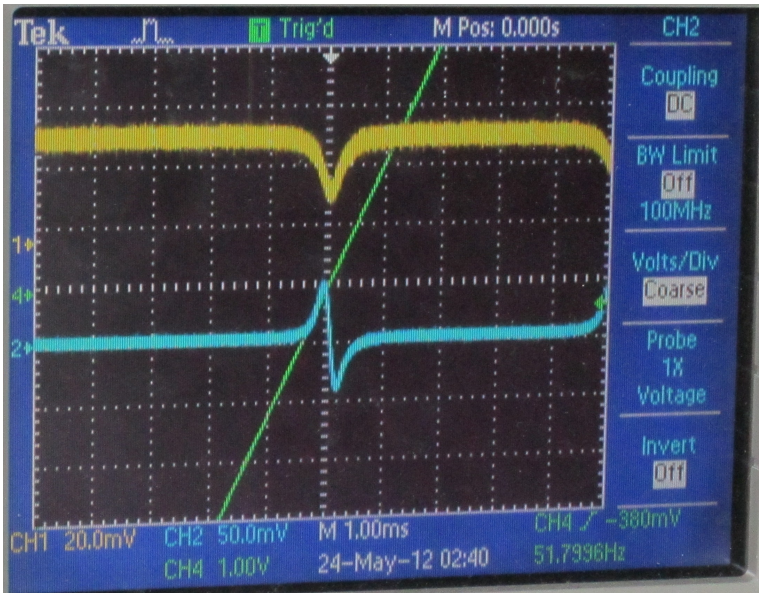

Figure A.1: The cavity and error signals for locking the cavity to the stable 780-nm laser

We send a beam of light from a 780-nm Toptica DLX-110 laser, which has been locked to the rubidium D_2 transition, into the cavity and monitor the reflected beam while scanning the piezo to create the peak to which we would like to lock. The Toptica laser is stabilized to a saturated absorption spectrum of ^{87}Rb using a method similar to Pound Drever Hall locking, where a Fabry Perot cavity signal is modulated and mixed with the modulation signal to provide an error signal. The saturated absorption spectrum signal is modulated and mixed with the modulation signal to create an error signal to which we lock. The stable light is transfered to the cavity via a polarization-maintaining fiber. Before inserting the 780-nm light into the cavity, we modulate it using an AOM to provide both the sidebands for locking via the Pound Drever Hall method, as well as a way to shift the lock point of the laser so that the cavity peaks of the 780-nm light and the 960-nm light occur at the

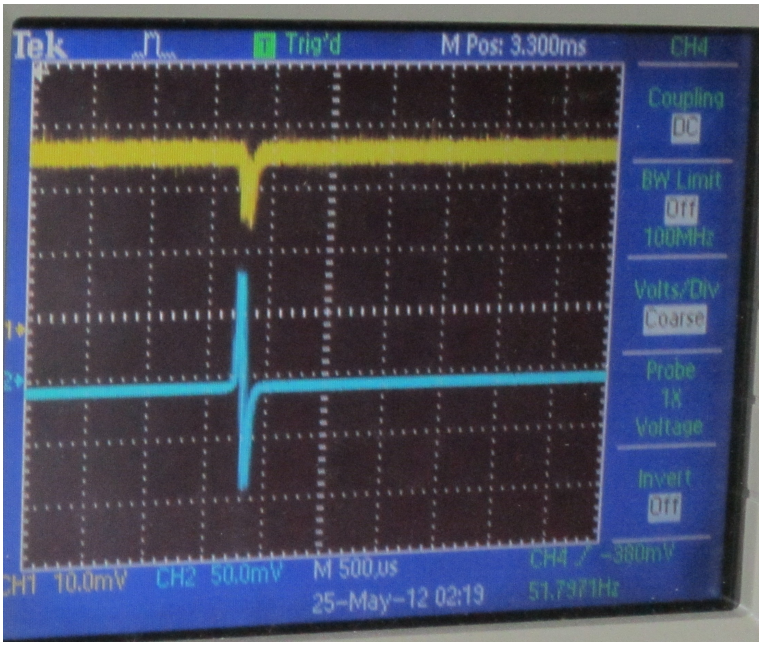

Figure A.2: The cavity and error signals for locking the 960-nm laser to the cavity.

same cavity length. We mix the modulation with the signal from the cavity to form a locking signal. Oscilloscope traces of the cavity and error signals are shown in Figure A.1. Using the AOM frequency scan, we can lock the cavity to the 780-nm laser and scan the lock point by a few tens of MHz.

A.3 Stabilization of the 960-nm laser

We stabilize the 960-nm laser by locking the master laser to the signal from the stabilized Fabry Perot cavity. We use a $\lambda/2$ plate and a polarizing beam splitter to split off a small amount of the amplified beam. This beam is sent through a fiber-coupled electro-optic modulator (EOM), which creates modulated sidebands on the light. This modulated light is then sent through a double-passed AOM to put sidebands on each of the sidebands from the EOM. The doubly-modulated light is

then sent into the cavity and the reflected signal is observed. The modulated signal is mixed with the RF modulation to create an error signal in the slow modulation regime [9]. We can lock to this signal by feeding back to two piezos that shift the grating in the master laser. Oscilloscope traces of the locking signals are shown in Figure A.2.

Because we lock to one of the EOM sidebands rather than the initial beam, we can shift the frequency of the 960-nm laser without affecting the locking signal. While the laser is locked, a Fluke digital RF signal generator is used to shift the frequency by up to 75 MHz in 1-MHz increments without unlocking the laser . It would also be possible to move in 100-kHz increments or smaller, but moving by increments larger than 1 MHz causes the laser to unlock, probably due to the width of the peak in the cavity signal, which is ~ 1 MHz. Because the free spectral range of our cavity is 150 MHz, when we have shifted 75 MHz, the two sidebands meet and the laser unlocks momentarily. Occasionally it will relock to the original sideband, but it can also relock to the opposite-polarity sideband. For this reason, we avoid shifting our blue light frequency more than 150 MHz, as the doubled light has twice the range as the 960-nm light.

A.4 Steps for Realigning the Doubler Cavity

Optimizing the blue light power is one of the trickiest parts of operating this experiment. Because the TA chip must occasionally be replaced, and the master-slave laser system must be realigned every time the grating is moved to change the

principal quantum number that we excite, it is frequently necessary to realign the beam that goes into the doubler cavity and re-optimize the generated blue light power. Here, I will describe the process I use to realign the doubler cavity, from scratch, along with tips to optimize power if the alignment is only slightly off.

All of these alignment procedures are performed with the TA current set to 1500 mA, until the final power optimization.

Before worrying about inserting the light into the doubler itself, I check the spatial mode of the beam and determine the divergence of the laser. I used a ThorLabs beam profiler to take beam profiles at various distances from the TA case. TA-amplified beams tend to improve in spatial mode as they propagate to the far field, so be sure to measure over a long range of distances. I place my first mode-matching optic over 1.5 m from the laser head. I take beam profiles with and without the optical isolator to ensure that the aperture of the isolator is not causing diffraction patterns in the beam.

Once I have measured the beam divergence and size, I can use Gaussian beam software, such as the Gaussian Beam Calculator, to determine the lenses I need to insert to create the desired waist at the desired position before the Wavetrain entrance. Refer to the figures and plots in the Wavetrain manual to determine what waists and positions are necessary.

After mode-matching optics are in place, I begin the alignment process. I remove the EOM that creates the sidebands for locking the doubler cavity at the beginning of alignment. I will have to reinsert this later before I can stabilize the blue light and measure its power. To begin the alignment, I ensure that the beams

are hitting roughly in the center of all the external mirrors. The beam is very large on the two mirrors immediately before the doubler cavity, as well as on the lens just before the doubler entrance and the doubler entrance itself. This is normal.

Next, I remove the top cover of the doubler and use a small IR fluorescence card or a strip of index card and a viewer to align the beam so that it is centered on both mirrors in the doubler. Because the mirrors are tilted in the cavity and the mounts are large, it will sometimes be necessary to align the beams so that they look like they are slightly off-center. If the cavity has been aligned recently, it is sometimes sufficient to align the beam with one mirror so that it enters the center of the doubler cavity aperture, and then to observe the transmitted light with an index card and an IR viewer. I can then adjust the second mirror to line up the beams exiting the cavity. There will be a flash of brighter light if this procedure alone provides cavity build up. In the event that this procedure is not sufficient to observe cavity build up peaks on the scope, I refer to the alignment procedure in the Wavetrain manual.

Once the cavity has been aligned to the point that I can see peaks on the oscilloscope, I adjust the yellow and red knobs on the top of the doubler to optimize the mode. The goal is both to minimize all but the main peak, as well as to increase the size of this peak. At operating currents applied to the TA driver, I can usually see a peak-to-peak voltage of 4-6 V, as shown in Figure A.3. With a cavity build up signal of 5 V, it should be possible to obtain 20-30 mW of blue light.

It is sometimes necessary to adjust the tilt and the position of the lens just outside the doubler entrance. Adjusting thiis lens will alter the beam alignment, so

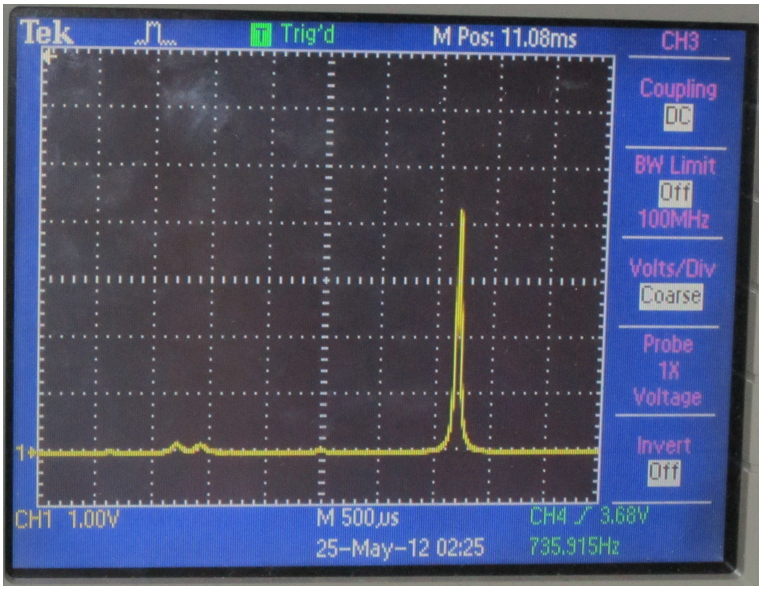

Figure A.3: The fundamental mode of the doubler cavity, showing the main mode with a peak-to-peak voltage of 4 V.

I always alternate adjustments of the tilt and position with adjustments of the last mirror before the doubler, in order to get an accurate idea of how I am improving mode build up.

Once the peaks are pretty optimized in size, I insert the EOM and try to lock the blue light. The peak-to-peak voltage of the cavity signal must be greater than 1 V for the cavity to lock stably, so I sometimes turn up the current to reach this. Upon locking the cavity for the first time, I often notice a series of horizontal fringes in the beam. These fringes indicates that the crystal tilt is off. Alternate adjusting the crystal tilt knob and the vertical adjustment (red knob) of the output mirror on the doubler to improve this.

This is the main procedure to get the power to a place where it can be optimized on a daily basis. Once the light locks and can be measured on a power meter,

optimize the power by iterating alignment of first the doubler mirrors and crystal tilt, then the tilt and position of the lens in front of the doubler, and then the two sets of external mirrors before the entrance to the doubler breadboard (before the EOM). Careful repetition of this sequence will cause the power to creep up. If the power stalls at a low level, consider gently cleaning the crystal.

A.5 Linewidth measurement via self-homodyne detection

The Rydberg transition is long-lived, which implies a narrow linewidth, <1 MHz. Our excitation times will therefore be limited by the linewidth of our laser system. We need to determine that our laser linewidth is as narrow as possible. As mentioned before, in a previous laser arrangement, we struggled with noise on the cavity and an broadband line shape. We use self-homodyne detection to determine the linewidth of our laser, which is self-heterodyne detection [41, 49] without the use of a modulator in one arm of the interferometer.

We make a self-homodyne signal by coupling the laser light into an optical fiber 50/50 beam splitter. The split beam is recombined in a second 50/50 fiber splitter and the output signal is measured on a fiber-coupled photodiode. This optical assembly forms a fiber-coupled Mach-Zender interferometer. In order to get linewidth information about the laser, we delay one arm of the interferometer by inserting a long length of fiber and creating a long path difference between the two arms before they are recombined. The signal from the photodiode is then sent to a spectrum analyzer and viewed to see the frequency scale on which the signal decays.

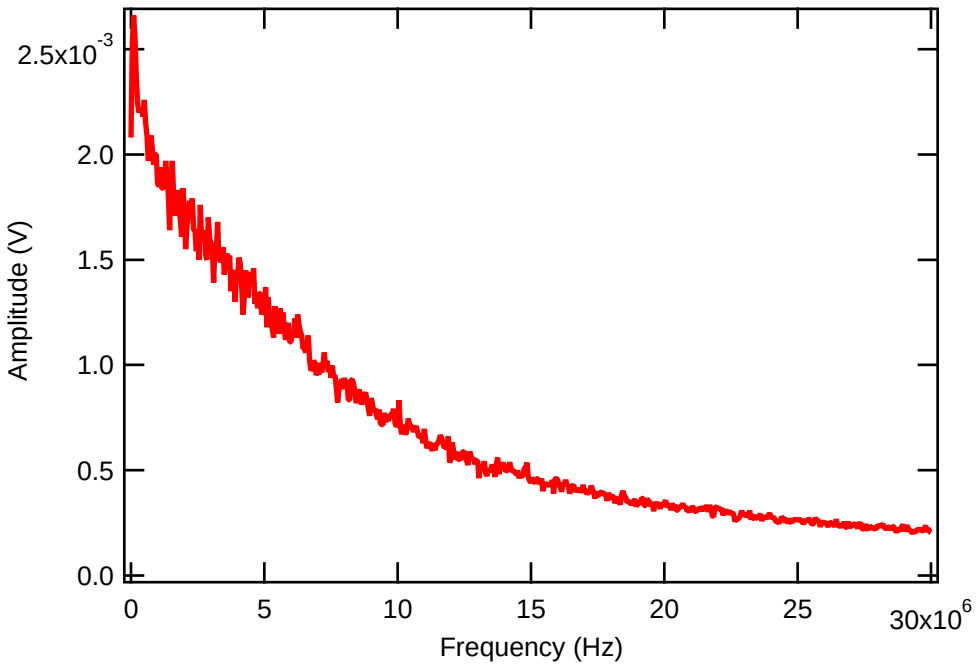

Figure A.4: The self-homodyne measurement of the Sacher Tiger laser before re-designing the system.

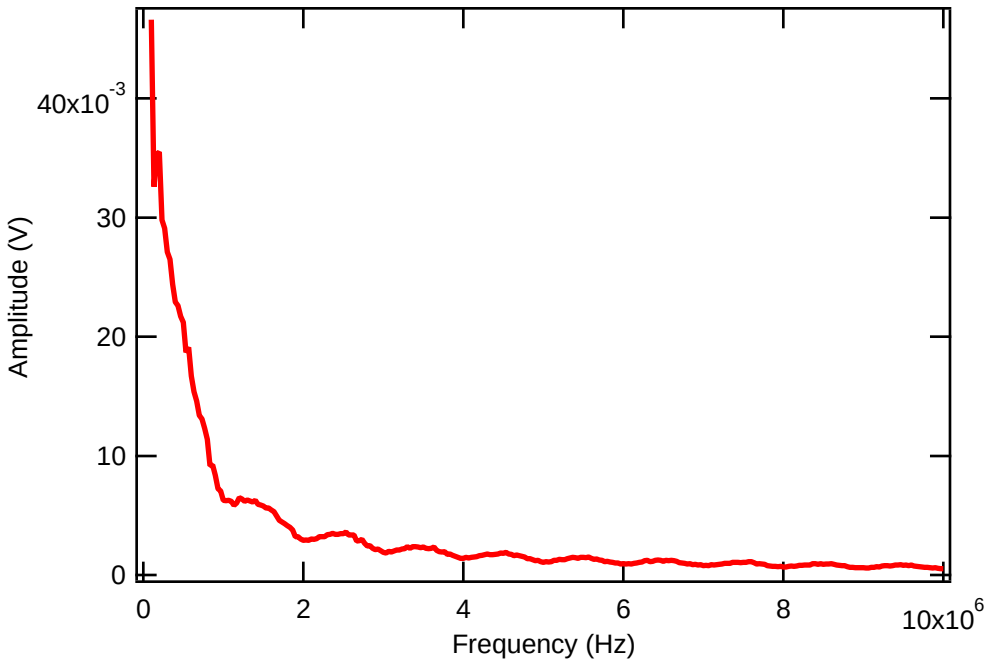

Figure A.5: The self-homodyne measurement of our 780-nm Toptica laser, to show the oscillations when the linewidth is smaller than the resolution of the self-homodyne detection.

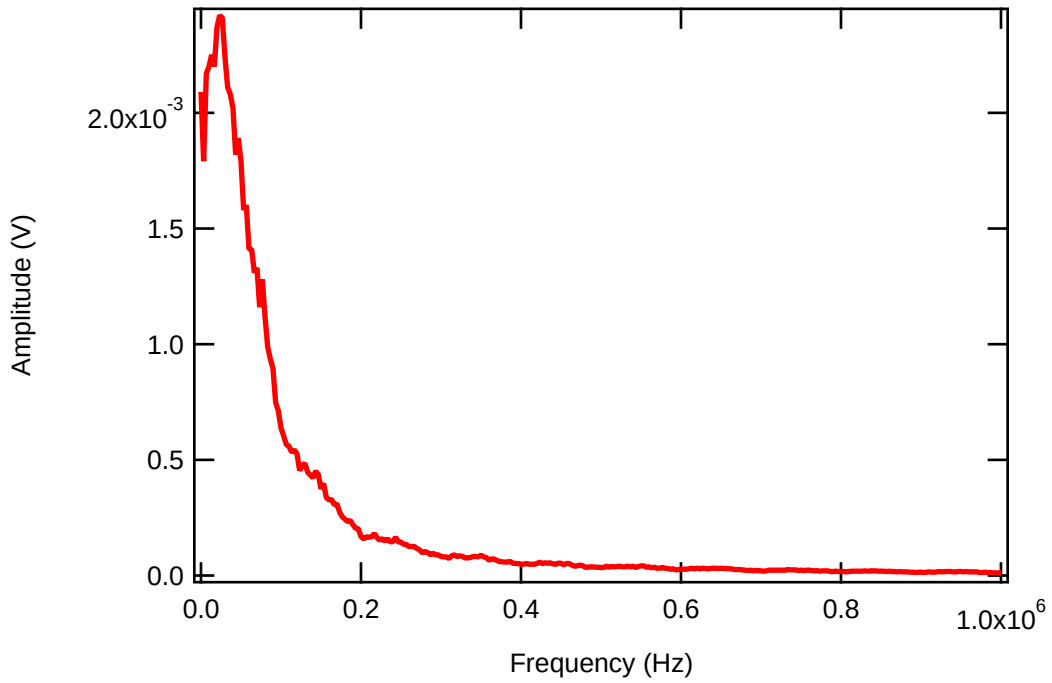

Figure A.6: The self-homodyne measurement of our home-built laser, used to pump the Sacher Tiger laser as an amplified system.

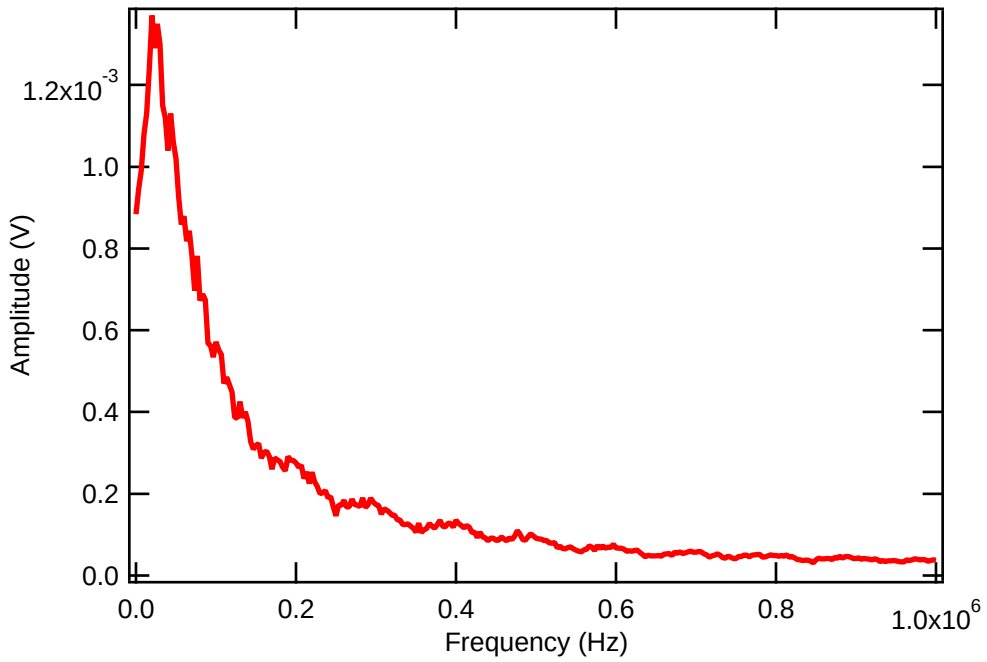

Figure A.7: The self-homodyne measurement of the amplified 960-nm laser, using the Sacher Tiger laser as an amplifier.

The signal on the spectrum analyzer will be somewhat obscured by the 1/f noise, but we can use the width of this signal to get a half-linewidth of the laser itself. Because the linewidth of the laser is related to its coherence length, the length of the delay line in the long arm of the interferometer limits the narrowest linewidth that we can measure. For our measurements, we have used fibers of 500-m length and 2-km length, yielding lower limits of 2 MHz and 500 kHz, respectively. Before changing the configuration of our laser system, we measured the linewidth of the Sacher TEC-300 to be $\sim$ 10 MHz, as shown in Figure A.4, while the linewidth of the Toptica laser was below 2 MHz, as shown in Figure A.5.

When the measured linewidth is below the lower limit due to the path length, the signal will take on periodic modulations, so we can be sure that the Toptica laser has a linewidth below 2 MHz, although we cannot determine the exact width. After changing the laser system, we measured both the homebuilt master laser and the amplified beam to have a linewidth of less than 500 kHz, measured by delaying the interferometer with a 2-km fiber. Figures A.6 and A.7 show these measurements. This shows that our new setup has improved the linewidth of our laser.

A.6 Rydberg Transition Wavenumbers

I calcuated Rydberg transition wavelengths from the expression in [21]

$$W_{nl} = -\frac{1}{2(n-\delta_l)^2}, \tag{A.1}$$

where δ_l is the quantum defect. This expression is calculated with respect from the continuum, so after converting from atomic units to SI units, I used it to determine the energy to excite from the $5P_{3/2}$ state to the Rydberg state by adding W_{nl} to the ionization limit energy. I then halved the values to take into account that I measure the wavenumber before doubling the light. Table A.1 shows the desired transition wavenumbers to the Rydberg states for the transitions I excited. The experimentally observed wavenumbers at which we saw transitions were within ~ 0.01 cm^{-1} of these calculated values. This small offset is due to both the ~ 300 MHz shift of the fiber EOM, which provides sidebands to lock the 960-nm light and a small, systematic offset of the wavemeter.

Table A.1: A table of wavenumbers used in the experiment. I have included the $n = 41, 50, 56$, and 61 values used in the experiment, as well as some nearby values to give a sense of the energy between Rydberg S states.

n	nS wavenumber (1/cm)
41	10398.8631
42	10400.8065
43	10402.6056
44	10404.2742
45	10405.8246
46	10407.2679
50	10412.1466
51	10413.1793
52	10414.1493
53	10415.0615
54	10415.9204
55	10416.7301
56	10417.4943
61	10420.7400

Appendix B

Electric Field Modelling

B.1 Overview

We used the program SIMION (application notes found at simion.com) to model our in-vacuum electrodes in order to determine a rough estimate of the magnitude and direction of the electric fields that we applied to our atoms. The arrangement of in-vacuum electrodes and optics allow for a simple way to apply a constant, vertical electric field with good homogeneity over the size of the cloud. In SIMION, the electrodes are modeled and the electric field can be read by hovering the mouse over the region in space where one wishes to know the calculated field at that point. Field lines can be approximated by simulating electron trajectories, but these are not exact. For all electrode configurations, voltages are applied to the simulated electrodes to give roughly 2 V/cm at the center of the gold mirror, and homogeneity is determined with these values.

B.2 Basic electrode arrangement

In the past, this chamber was used to trap atoms from rubidium dispensers still present in the chamber [17]. Because the feedthroughs still exist to apply voltage to these dispensers, we were able to alter their configuration to act as electrodes

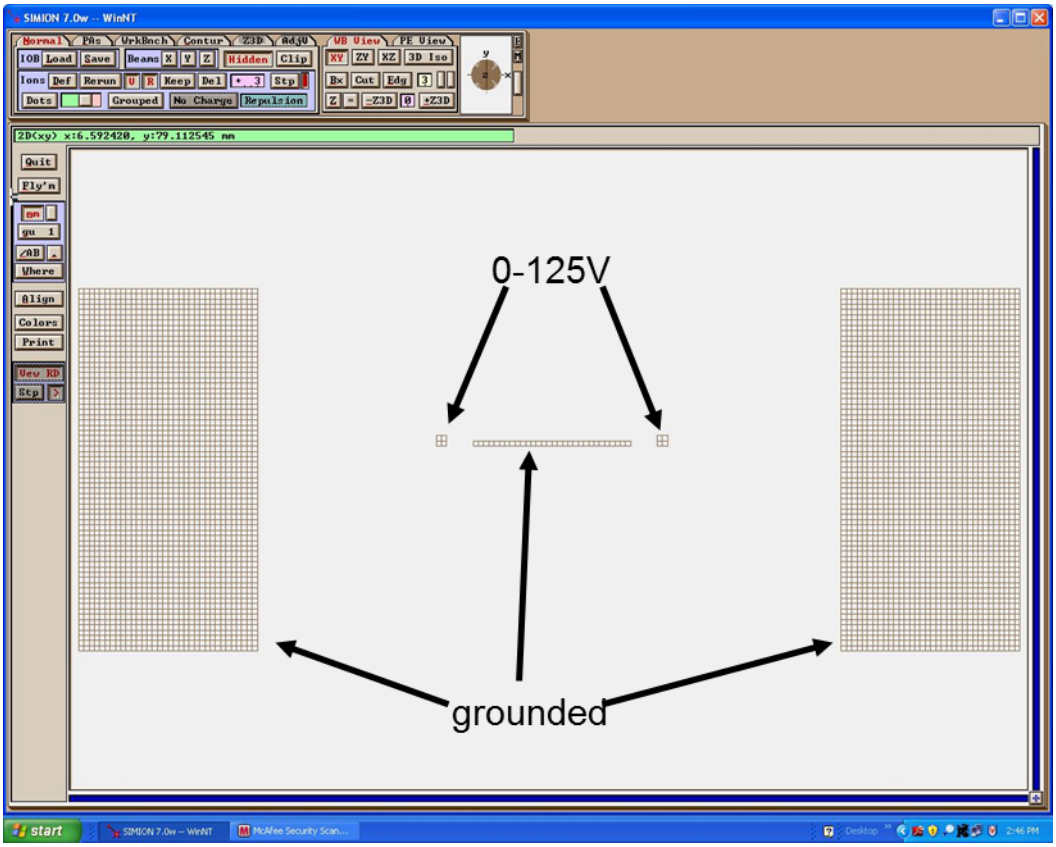

Figure B.1: SIMION simulation of the in-vacuum electrodes, projected onto a 2-D plane.

rather than dispensers. By disconnecting the dispensers from one feedthrough and repositioning them, we can apply voltage without the risk of running a current that would cause dispensation of rubidium in the chamber. In Chapter 4, I showed a photograph of the in-vacuum components, with the dispensers redesigned to act as field electrodes.

B.3 SIMION simulation of ion trajectories and charge accumulation

We can model this electrode arrangement using the program SIMION. We simplify the setup by taking a 2-dimensional slice in the xz plane. We can model the grounded gold mirror as a thick piece of grounded conductor, the chamber walls as grounded conductors, and the plane of the optics table as a grounded conductor and then insert electrodes with varying voltages and positions at the approximate positions of the in-vacuum electrodes. This simulation setup is shown in Figure B.1. We can use the program to estimate the magnitude of the electric field at the center of the gold mirror and can use this estimate to determine how the electrode configuration affects the homogeneity of the field along the plane of the mirror. Note that the in-vacuum electrodes extend along the mirror on two sides, providing excellent homogeneity along the surface of the mirror in the y direction.

B.4 Rejected electrode configurations

Because of the risk of charge accumulation, we had several iterations of electrode designs. In this section, I will briefly describe past electrode configurations and give the reasons that these configurations were rejected or abandoned.

B.4.1 Electrode outside chamber

The first electrode configuration involved applying voltage to a 4"-diameter copper gasket, which was mounted below the chamber, outside of the vacuum. Figure B.2 shows a 2-dimensional slice of this setup, considering the arrangement to be

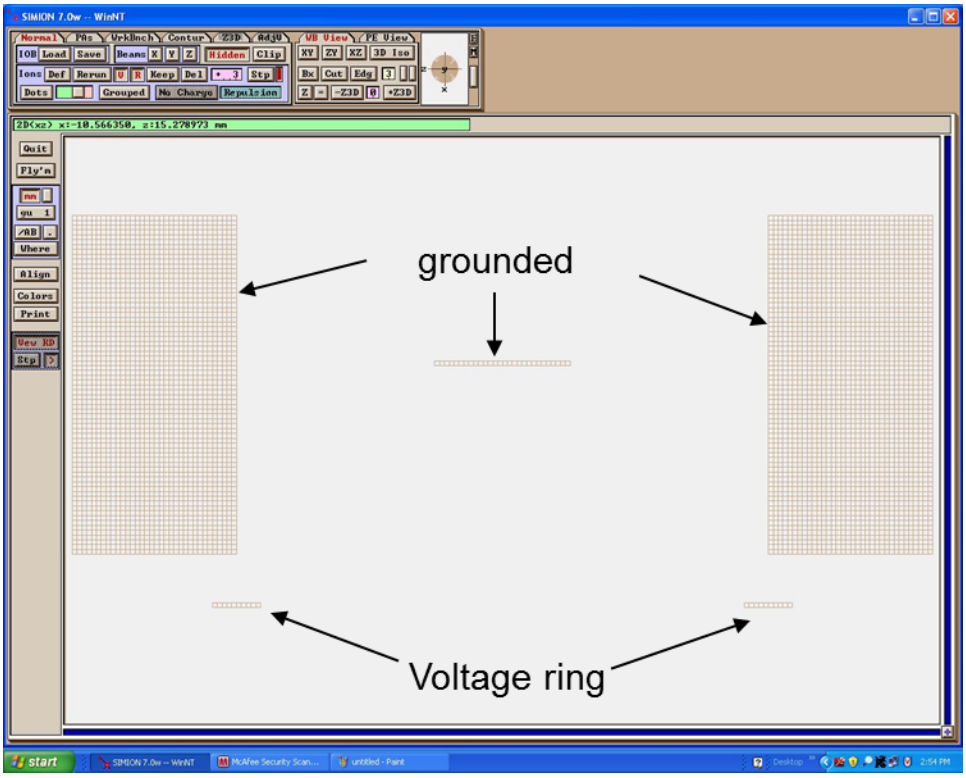

Figure B.2: SIMION simulation of the initial electrode configuration, with the voltage applied to a ring-shaped electrode outside the chamber.

approximately cylindrically symmetric. This configuration provided a strong vertical electric field at the surface of the gold mirror with reasonable applied voltages. Additionally, we had to consider the field between the electrode and the edges of the vaccum chamber where we mounted it, to ensure that the electric field at the edges was not large enough to cause dielectric breakdown of the air and arcing.

We discovered that with this electrode configuration, we experienced a time-variation of the electric field effect, most likely due to accumulation of charged ions on the dielectric window at the bottom of the chamber. We also were concerned that polarization of the mirror itself could lead to further field screening.

B.4.2 Single in-vacuum electrode

After discovering the issues with charge accumulation and screening from the external electrode, we implemented an electrode configuration taking advantage of the in-vacuum electrodes near the gold mirror. Because the gold mirror is a grounded conducting plane, the field will be perpedicular to its surface regardless of the location of the voltage source. We originally applied voltage to a single in-vacuum electrode, producing an electric field with a large degree of variability in the plane parallel to the mirror.

This inhomogeneity of the field was significant over the size of the MOT and resulted in a strong broadening of the Autler-Townes signal for increasing electric field. While this effect was initially believed to be due to the dipole-dipole interaction, we later discovered that the $\sim 20\%$ variation of the field over the size of the

MOT could result in such broadening. This broadening was reduced significantly by applying voltage to two electrodes in a more symmetric configuration, as described above.

B.4.3 Two opposite-sign in-vacuum electrodes

In order to prevent the accumulation of charges on the bottom window, even with the in-vacuum electrodes, we considered applying opposite-sign voltages to each of the two electrodes so that there was no component of the electric field that directed the ions/electrons straight downwards. We abandoned this configuration before implementing it in the experiment, as we realized that such a configuration would create a greater field inhomogeneity than any other arrangement.

Bibliography

[1] S. E. Anderson, K. C. Younge, and G. Raithel, *Phys. Rev. Lett.*, **107**, 263001 (2011).

[2] Ilya Arakelyan, *Two Experiments with Cold Atoms: II. Spectroscopic Measurements of Rydberg Blockade Effect*, Ph. D. Thesis, University of Maryland, 2009.

[3] Ennio Arimondo, private communication.

[4] G. E. Astrakharchik, J. Boronat, I. L. Kurbakov, and Yu E. Lozovik, *Phys. Rev. Lett.*, **98**, 060405 (2007).

[5] S. H. Autler and C. H. Townes, *Phys. Rev.*, **100**, 703-722 (1955).

[6] Matthew Charles Beeler, *Disordered Ultracold Two-Dimensional Bose Gases*, Ph. D. Thesis, University of Maryland, 2011.

[7] I. I. Beterov, et al., *New J. Phys*, **11**, 013052 (2009).

[8] I. I. Beterov, et al., *Phys. Rev. A*, **79**, 052504 (2009).

[9] Eric D. Black, *Am. J. Phys.*, **69**, 79 (2001).

[10] Immanuel Bloch, Jean Dalibard, and Wilhelm Zwerger, *Rev. Mod. Phys.*, **80**, 885964 (2008).

[11] H. P. Büchler, et al., *Phys. Rev. Lett.*, **98**, 060404 (2007).

[12] F. Cinti, et al., *Phys. Rev. Lett.*, 105 135301

[13] C. Cohen-Tannoudji, Jacques Dupont-Roc, and Gilbert Grynberg, *Atom-Photon Interactions: Basic Processes and Applications* (John Wiley & Sons, New York, 1992).

[14] J.-P. Connerade, *Physica Scripta*, **68**, C25 (2003).

[15] W. E. Cooke and T. F. Gallagher, *Phys. Rev. A*, **21**, 588 (1980).

[16] Timothy P. Dinneen, Christopher D. Wallace, Kit-Yan N. Tan, and Phillip L. Gould, *Optics Letters*, **17**, 1706 (1992).

[17] Emily E. Edwards, *Construction of Apparatus and First Experiments Investigating Dynamics of Bose-Einstein Condensates in Disordered Opitcal Lattices*, Ph. D. Thesis, University of Maryland, 2009.

[18] Matthew P. A. Fisher, Peter B. Weichman, G. Grinstein, and Daniel S. Fisher, *Phys. Rev. B*, **40**, 546-570 (1989).

[19] C. Gabbanini, F. Ceccherini, S. Gozzini, and A. Lucchesini, *J. Phys. B*, **31**, 4143-4148 (1998).

[20] Alpha Gaëtan, et al., *Nature Physics*, **5**, 115-118, (2009).

[21] T. F. Gallagher, *Rydberg Atoms* (Cambridge University Press, Cambridge, England, 1994).

[22] T. F. Gallagher and W. E. Cooke, *Phys. Rev. Lett.*, **42**, 835 (1979).

[23] K. Goral, L. Santos, and M. Lewenstein, *Phys. Rev. Lett.*, **88**, 170406 (2002).

[24] H. R. Gray and C. R. Stroud, Jr., *Optics Communications*, bf 25(3), 359-362 (1978).

[25] M. Greiner, et al., *Nature*, Vol. 415, pp. 39-44 (2002).

[26] Axel Griesmaier, et al., *Phys. Rev. Lett.*, **94**, 160401 (2005).

[27] Rudolf Grimm, M. Weidemüller, and Y. B. Ovchinnikov, *Adv. Atom. Mol. Opt. Phy.*, **42**, 95 (2000).

[28] A. Haase, D. Cassettari, B. Hessmo, and J. Schmiedmayer, *Phys. Rev. A*, **64**, 043405 (2001).

[29] N. Henkel, R. Nath, and T. Pohl, *Phys. Rev. Lett.*, **104**, 195302 (2010).

[30] Gerhard Herzberg, *Molecular Spectra and Molecular Structure: I. Diatomic Molecules* (Prentice-Hall, Inc., New York 1939).

[31] Jens Honer, Hendrik Weimer, Tilman Pfau, and Hans Peter Büchler, arXiv:1004.2499v1 [cond-mat.quant-gas]

[32] D. Jaksch, C. Bruder, J. I. Cirac, C. W. Gardiner, and P. Zoller, *Phys. Rev. Lett.*, **81**, 3108 (1998).

[33] J. E. Johnson and S. L. Rolston, *Phys. Rev. A*, **82**, 033412 (2010).

[34] E. Kim and M. H. W. Chan, *Science*, **305**(5692), 1941-1944 (2004).

[35] T. Koch, T. Lahaye, J. Metz, B. Fröhlich, A. Griesmaier, and T. Pfau, *Nature Physics*, **4**, 218-222 (2008).

[36] C. Kollath, J. S. Meyer, and T. Giamarchi, *Phys. Rev. Lett.*, **100**, 130403 (2008).

[37] W. H. Li, I. Mourachko, Michael Noel, T. F. Gallagher, *Phys. Rev. A*, **67**, 052502 (2003).

[38] J. R. Lowell, et al., *Phys. Rev. A*, **66**, 062704 (2002).

[39] F. Maucher, et al., arxiv:1102.2121v1

[40] Kaushik Mitra, C. J. Williams, C. A. R. Sà de Melo, arXiv:0903.4655v1 [cond-mat.other] (2009).

[41] T. Okoshi, K. Kikuchi, and A. Nakayama, *Electron. Lett.*, **16**(16), 630-631 (1980).

[42] M. Ortner, A. Micheli, G. Pupillo, P. Zoller, *New J. Phys*, 11, 055045 (2009)

[43] Pfau, Tilman, "Coherent control of dense Rydberg gases." Joint Quantum Institute Seminar, College Park, MD, 11 June 2012.

[44] William D. Phillips and Harold Metcalfe, *Phys. Rev. Lett.*, **48**, 596-599 (1982).

[45] E. J. Pratt, et al., *Science*, **332**(6031), 821-824 (2011).

[46] G. Pupillo, et al., arXiv:0904.2735v1 [cond-mat.quant-gas] (2009).

[47] G. Pupillo, et al., *Phys. Rev. Lett.*, **104**, 223002 (2010).

[48] Ulrich Raitzsch, et al., *Phys. Rev. Lett.*, **100**, 013002 (2008).

[49] L. E. Richter, H. I. Mandelberg, M. S. Kruger, and P. A. McGrath, *Quant. Electron. Lett.*, **QE-22**(11), 2070-2074 (1986).

[50] J. J. Sakurai, *Modern Quantum Mechanics* (Addison-Wesley, Reading, Mass., 1994).

[51] V. W. Scarola and S. Das Sarma, *Phys. Rev. Lett.*, **95**, 033003 (2005).

[52] Arne Schwettmann, Jeff Crawford, K. Richard Overstreet, and James P. Shaffer, *Phys. Rev. A*, **74**, 020701 (2006).

[53] Peter W. Shor, *SIAM J.Sci.Statist.Comput.*, **26**, 1484 (1997).

[54] Kilian Singer, Jovica Stanojevic, Matthias Weidemüller, and Robin Côté, *J. Phys. B*, **38**, S295-S307 (2005).

[55] Andrew Steane, *Rep. Prog. Phys.*, **61**, 117 (1998).

[56] Daniel Adam Steck, *Rubidium 87 D Line Data*, online at http://steck.us/alkalidata/

[57] D. Tong, et al., *Phys. Rev. Lett.*, **93**, 063001 (2004).

[58] E. Urban, et al., *Nature Physics*, **5**, 110-114, (2009).

[59] Thibault Vogt, et al., *Phys. Rev. Lett.*, **99**, 073002 (2007).

[60] Thad Walker and Mark Saffman, *J. Phys. B: At. Mol. Opt. Phys.*, **38**, S309, (2005).

[61] H. E. White, *Introduction to Atomic Spectra* (McGraw-Hill Book Company, Inc., New York 1934).

[62] M. Zimmerman, M. G. Littman, M. M. Kash, and D. Kleppner,*Phys. Rev. A*, **20**, 2251 (1979).